

Improving Interpretable Piecewise Linear Models through Hierarchical Spatial and Functional Smoothing

Philip A. White ^{*1}, Durban G. Keeler ^{†2}, Daniel Sheanshang^{‡1}, and Summer
Rupper ^{§2}

¹Department of Statistics, Brigham Young University, USA

²Department of Geography, University of Utah, USA

September 23, 2020

Abstract

Scientists often use simple models with solutions that provide insight into physical and environmental systems. Although easy to understand, these simple models often lack the flexibility to accurately model associated data. We focus on the setting where we have functional data distributed over space, where (1) the interpretable model can be expressed as a linear combination of basis functions, (2) the properties of the data-generating process vary spatially, and (3) the interpretable model is too simple to effectively match the data. In this manuscript, through our motivating example of modeling snow density, we develop a framework for functionally smoothing generalized piecewise linear models while preserving inference on the simple model by projecting a smooth function into the orthogonal column space of the piecewise linear model. Moreover, we allow the parameters of the simple model and the functional smoothing to vary spatially.

*Corresponding Author: pwhite@stat.byu.edu

†durban.keeler@gmail.com

‡danielsheanshang@gmail.com

§summer.rupper@geog.utah.edu

We use a snow density model for ice sheets as the motivating application of this model. The underlying piecewise linear differential equation solution fails to match several data features. We address these issues with a novel, physically-constrained regression model for snow density as a function of depth. The proposed spatially and functionally smoothed snow density model better fits the data while preserving inference on physical parameters. Lastly, we use a unique hierarchical, heteroscedastic error model that accounts for differences between data sources. Using this model, we find significant spatial variation in the parameters that govern snow densification.

KEYWORDS: Bayesian statistics, differential equation, firn density, functional data, Gaussian process, piecewise linear, spatial statistics

1 Introduction

The physical sciences frequently use simple piecewise linear (or even piecewise constant) functions to model spatially-varying physical phenomena, often in the context of linear differential equations. When modeled with uncertainty, we can express such models in the general form of

$$\begin{aligned} y(\mathbf{s}, x) &\sim f(\mu(\mathbf{s}, x)), \\ \mu(\mathbf{s}, x) &= g^{-1}(\alpha(\mathbf{s}) + \mathbf{z}(x)^T \mathbf{k}), \end{aligned} \tag{1}$$

where $f(\cdot)$ is a probability density that allows the data to deviate from an intentionally simple and interpretable mean or location function $\mu(\mathbf{s}, x)$ indexed by location \mathbf{s} and another functional quantity x (e.g., time or depth). The mean is specified by a link function $g(\cdot)$, a spatially-varying intercept $\alpha(\mathbf{s})$, and linear combinations of j basis functions $\mathbf{z}(x) = (z_1(x), \dots, z_j(x))^T$ with coefficients $\mathbf{k} = (k_1(x), \dots, k_j(x))^T$. Models of this form are appealing because the corresponding coefficients \mathbf{k} are easy to interpret, often computationally cheap, and many differential equation models have solutions of this form. Although not limited to these domains, examples of this modeling framework are plentiful in the environmental and climate science literature. In climate change modeling, piecewise constant or linear models to infer trends in climate parameters are common (see, e.g., [Pawson et al., 1998](#); [Tomé & Miranda, 2004](#); [Seidel & Lanzante, 2004](#); [Tebaldi & Sansó, 2009](#); [Schofield et al., 2016](#); [Banesh et al., 2019](#)). Additional examples are present in soil water content modeling ([Chen et al., 2014](#); [Koster et al., 2020](#)), estimating effects of climate change on food produc-

tion (Katz, 1977; Tebaldi & Lobell, 2008; Ortiz-Bobea & Tack, 2018), understanding human impacts on landscape ecology (Horner et al., 2009; Howarth et al., 2012), hydrological predictions and risk assessments (Das Bhowmik et al., 2018; Dai et al., 2019), and quantifying environmental impacts on economies (Engle et al., 1986; Du et al., 2017).

These simple models can miss important data features because (1) piecewise linear models fail to capture nonlinearities in smoothly varying processes and (2) spatially invariant models fail to estimate how physical processes change over space. Because basis functions $\mathbf{z}(x)$ and corresponding coefficients \mathbf{k} either do not vary over space or do not incorporate spatial autocorrelation, this assumption may be inappropriate if aspects of the data generating process (e.g., the physical system, environment, or climate) vary over space or have spatial autocorrelation. Such conditions are nearly universally applicable in Earth and environmental sciences. The inherent spatial variability and autocorrelation are further complicated because, depending on the application, components of \mathbf{k} may not be identifiable from a single site or constrained to physically plausible values. In this paper, we provide two novel contributions to address potential shortcomings of the framework presented in (1). Although these contributions are more generally applicable, we focus our discussion on the motivating example of snow density modeling in West Antarctica because (1) Antarctic snow density models and data illustrate the issues discussed and (2) accurately estimating Antarctic snow density is an important scientific target given the importance of understanding the response of the world’s largest fresh water reservoir to climate change and its contributions to sea level rise.

First, we propose an extension of the spatially varying coefficient model (Gelfand et al., 2003) to meet the interpretable constraints of \mathbf{k} , possibly allowing basis functions $\mathbf{z}(x)$ to vary spatially, and to resolve potential identifiability issues while allowing \mathbf{k} to vary by location \mathbf{s} (see Section 3.1). As a second contribution, we add a flexible, spatially-correlated functional component to $g(\mu(\mathbf{s}, x))$ to improve the fit to the data while preserving inference on the parameters in \mathbf{k} . While functional models are often used in conjunction with linear components (see Heckman, 1986, for early discussion), functional components can interfere with inference on \mathbf{k} when these model components are fit jointly. To preserve inference on the parameters in \mathbf{k} , we project the functional component into the orthogonal column space of the basis functions $\mathbf{z}(x)$ (see Section 3.2), an approach that is conceptually similar to spatial-confounding models (see, e.g., Hodges & Reich, 2010; Paciorek, 2010; Hughes & Haran, 2013). Together,

these two contributions improve simple and interpretable models by (1) allowing parameters and basis functions to vary spatially and (2) smoothing the interpretable piecewise linear model to better fit the data while not interfering with inference on physical parameters.

In our motivating problem, we observe snow¹ density measurements as a function of depth taken from 57 snow cores drilled at 56 sites over West Antarctica and wish to estimate snow density as a function of depth. Antarctic snow density estimation is essential for multiple outstanding questions in the polar sciences. For instance, snow density measurements, combined with remote sensing data, allow scientists to reconstruct snow precipitation over the recent past (see e.g., [Medley et al., 2014](#); [Koenig et al., 2016](#); [Lewis et al., 2019](#); [Keeler et al., 2020](#)). Scientists also use radar and laser altimetry to measure elevation changes over Antarctica and translate these measurements into mass differences using snow density estimates (see e.g., [Li & Zwally, 2011](#); [Csatho et al., 2014](#); [Shepherd et al., 2019](#); [Smith et al., 2020](#)). Understanding such mass losses and precipitation changes are primary research targets within the scientific community, with critical implications for current and future sea-level rise ([IPCC, 2013](#)). Importantly, no current remote sensing techniques permit the estimation of snow density, necessitating reliance on in-situ measurements. Due to the remoteness and extreme environments of Antarctica, such measurements are costly to obtain, making improved utilization of existing data of paramount concern ([Eisen et al., 2008](#)).

We, therefore, propose improvements to typical piecewise linear differential equation models used in estimating snow density with depth through functional smoothing on the depth scale x and by spatial smoothing. We use a novel constrained, multivariate spatial model motivated by the physics of densification (See [Section 2.1](#)) and data attributes discussed in [Section 2.2](#). This model resolves the identifiability issues of current models through multivariate spatial smoothing or information sharing. To capture the appropriate constraints on snow density and physical parameters, we specify a multivariate Gaussian process model in a transformed parameter space and constrain the mean between 0 g/cm^3 and the density of ice $\rho_I = 0.917 \text{ g/cm}^3$. From an inferential perspective, our spatial model allows us to spatially interpolate physical quantities whose spatial properties are currently poorly understood.

We continue by discussing the snow densification processes and our snow density dataset in [Section 2](#). In this section, we also fit the [Herron & Langway \(1980\)](#) model without adaptations to motivate the need for spatial and functional smoothing for these data (see, e.g.,

¹In the scientific literature, seasonally-persistent snow is called firn.

Hörhold et al., 2011; Verjans et al., 2020, for examples of more recent use). In Section 3, we present our modeling framework based on the physics and data attributes discussed in Section 2 that incorporates spatial and functional smoothing to an otherwise piecewise linear global model. In Section 4, we give our model comparison approach (Section 4.1), our final model (Section 4.2), as well as details on our prior distributions, model fitting, and prediction (Section 4.3). Based on our final model, we present results in Section 5. The data and code that support the findings of this study are openly available at https://github.com/philawhite/Piecewise_linear_smoothing.

2 Snow Densification Processes and Data

2.1 The Physics of Snow Densification

Snow densification is a thermal reaction with a temperature-dependent reaction rate called an *Arrhenius* constant k (corresponding to the regression slopes \mathbf{k} in (1)), defined as

$$k = Ae^{-\frac{E}{RT}}, \quad (2)$$

where T is the temperature (in Kelvin), $R \approx 8.314 \text{ J K}^{-1} \text{ mol}^{-1}$ is the ideal gas constant, $E > 0$ is the energy of activation, and $A > 0$ is a pre-exponentiation factor. A snow core extends from the surface of the ice sheet to some depth (2 to 140 meters in this dataset) beneath the surface, and density measurements are then taken along the full depth profile of the core. For a single snow core with many snow density estimates, the Arrhenius constant k is statistically identifiable, but parameters A and E that define k are not. Therefore, many cores with different temperatures are needed to identify A and E , a process that could be carried out regionally to account for geographic differences. However, such regional core groupings are arbitrary. Snow densification models also rely on surface mass balance (SMB), the average rate of snow accumulation, in m w.e./yr (meters water equivalent per year) because increased snowfall increases snow compaction rates.

Densification rates with depth change at various *critical densities* due to the interplay of particle rearrangement and plasticity change (Gow, 1975; Herron & Langway, 1980; Maeno & Ebinuma, 1983; Martinerie et al., 1992; Salamatin et al., 2009). Densification models often use three critical densities (Hörhold et al., 2011), giving a piecewise linear model

with four stages, each with a unique temperature-dependent slope corresponding to the densification rate over depth. In this manuscript, we focus on extensions of the interpretable [Herron & Langway \(1980\)](#) model (which we call the HL model), a highly cited and commonly used snow density model (see [Hörhold et al., 2011](#); [Verjans et al., 2020](#), as an example of recent use). Like many other models, the HL model can be written as a linear combination of piecewise linear basis functions on a transformed scale as in (1). From these data, we wish to estimate densification rates over depth, infer change points in density where densification rates change, and estimate temperature-dependent physical subcomponents of the densification rate (discussed in Section 3).

The HL model is defined in stages, where the behavior of the model changes at critical densities where various physical forces alter the pattern of densification (see [Hörhold et al., 2011](#), for review and discussion). The HL model defines rates of densification using Arrhenius constants for two stages: for densities less than 0.55 g/cm³ and between 0.55 g/cm³ and 0.80 g/cm³. The model is

$$\begin{aligned} \rho_I k_1 x + \log \left(\frac{y(0)}{\rho_I - y(0)} \right), & \quad \text{for } x \in [0, \kappa_1), \\ \frac{\rho_I k_2 (x - \kappa_1)}{\sqrt{SMB}} + \log \left(\frac{y(\kappa_1)}{\rho_I - y(\kappa_1)} \right), & \quad \text{for } x \in [\kappa_1, \kappa_2), \end{aligned} \quad (3)$$

where $k_1 = 11 \exp \{-10160/RT\}$, $k_2 = 575 \exp \{-21400/RT\}$, and T is the temperature 10-m below the surface. Depths κ_1 and κ_2 corresponding to the densities 0.55 and 0.80 g/cm³ can be extracted from (3) as

$$\begin{aligned} \kappa_1 &= \frac{1}{\rho_I k_1} \left[\log \left(\frac{0.55}{\rho_I - 0.55} \right) - \log \left(\frac{y(0)}{\rho_I - y(0)} \right) \right], \\ \kappa_2 &= \kappa_1 + \frac{\sqrt{SMB}}{\rho_I k_2} \left[\log \left(\frac{0.80}{\rho_I - 0.80} \right) - \log \left(\frac{0.55}{\rho_I - 0.55} \right) \right]. \end{aligned} \quad (4)$$

When comparing the HL model to field data, [Hörhold et al. \(2011\)](#) find good agreement to data at some sites and poor agreement at other sites. Fitting site-specific HL models, we observe similar issues for our data. Moreover, we find spatial patterns in the surface densities and the Arrhenius constants, as we discuss in Section 2.2. For these reasons, we propose spatially-varying extensions of (3) in Section 3.

More recent models for deeper snow cores often assume that there are three critical

densities at 0.55, 0.73, and between 0.82 – 0.84 g/cm³ (see [Hörhold et al., 2011](#), for review and discussion), which we call ρ_1 , ρ_2 , and ρ_3 . For each critical density, ρ_1 , ρ_2 , and ρ_3 , there is a corresponding critical depth κ_1 , κ_2 , and κ_3 . Using high-resolution density measurements, [Hörhold et al. \(2011\)](#) find that the first critical density ρ_1 ranged between 0.45 and 0.60 g/cm³ depending on the site, rather than always occurring at 0.55 g/cm³. Moreover, [Hörhold et al. \(2011\)](#) argue that the density transitions at critical densities ρ_2 and ρ_3 are only “weakly apparent.”

Rather than a two-stage model, we use a four-stage model that incorporates more recent extensions of the HL model with three random critical densities ρ_1 , ρ_2 , and ρ_3 . As discussed, because the transitions at ρ_2 and ρ_3 are weak, we assume that the hierarchical mean parameters for the second, third, and fourth stages are equal, but we do not constrain the site-specific parameters to be equal. We connect the physical and statistical models by writing the four-stage version of (3) as a generalized piecewise linear multiple regression model. Let α be an intercept, $\mathbf{z}(x)$ be depth-specific covariates with corresponding Arrhenius constants \mathbf{k} , and $\mathbf{1}(\cdot)$ be the indicator function. The model can be written as

$$\begin{aligned}
 \log\left(\frac{y(x)}{\rho_I - y(x)}\right) &= \alpha + \mathbf{z}(x)^T \mathbf{k}, & \alpha &= \log\left(\frac{y(0)}{\rho_I - y(0)}\right) \\
 z_1(x) &= \rho_I \min(x, \kappa_1), & z_3(x) &= \frac{\rho_I \min(x - \kappa_2, \kappa_3 - \kappa_2)}{\sqrt{SMB}} \mathbf{1}(x > \kappa_2), \\
 z_2(x) &= \frac{\rho_I \min(x - \kappa_1, \kappa_2 - \kappa_1)}{\sqrt{SMB}} \mathbf{1}(x > \kappa_1), & z_4(x) &= \frac{\rho_I (x - \kappa_3)}{\sqrt{SMB}} \mathbf{1}(x > \kappa_3).
 \end{aligned} \tag{5}$$

Although frequently assumed to be constant over spatial domains ([Herron & Langway, 1980](#); [Hörhold et al., 2011](#); [Verjans et al., 2020](#)), the physics related to thermal reaction rates and critical densities depend on snow type and conditions which change spatially ([Alley et al., 1982](#); [Johnson, 1998](#); [Freitag et al., 2004](#)). Therefore, Arrhenius constants and critical densities are not constant over space, something discussed by [Hörhold et al. \(2011\)](#) and in Section 2.2. Despite these findings, many current models rely on simple global fitting constraints averaged across all sites, often spanning both poles ([Herron & Langway, 1980](#); [Helsen et al., 2008](#); [Arthern et al., 2010](#); [Verjans et al., 2020](#)). Capturing the spatial variation in these parameters would therefore improve the accuracy and general applicability of snow density models to more widespread regions. In Section 4.2, we present the hierarchical spatial model corresponding to (5).

2.2 Data

This dataset consists of $N = 14,844$ density measurements from 57 snow/ice cores at $n_s = 56$ unique locations. These data come from four different field campaigns: the East Antarctic Plateau (Albert et al., 2004), the Siple Dome project (Lamorey & Cooper, 2002), the Satellite Era Accumulation Traverse (Burgener et al., 2013), and the US portion of the International Trans-Antarctic Scientific Expedition (Mayewski et al., 2005). We refer to these field campaigns as EAP, SDM, SEAT, and US-ITASE, respectively.

We denote density measurements as $y(\mathbf{s}_{ij}, x) > 0$ and the drilled core as \mathbf{s}_{ij} , where \mathbf{s}_i indicates the observed core location, j indexes replicates at the same site, and x represents depth. We let \mathcal{S} denote the collection of the 56 core sites \mathbf{s}_i . Because we use our model to estimate parameters where we do not have data, we let \mathbf{s} represent a generic spatial location. To specify campaign-specific parameters, we define $m(\mathbf{s}_{ij})$ to be an indicator for which field campaign acquired core \mathbf{s}_{ij} .

The precise methods and techniques of density measurement are generally similar but differ somewhat across campaigns. Density measurements involve measuring the mass and volume of sections of a core. Density measurements are averaged over some length of the snow core; therefore, density variability relies not only on the mass and volume measurements themselves but also on the length of the core section used. We let $dx_{\mathbf{s}_{ij}}$ be the length of the core used to procure a density measurement for core \mathbf{s}_{ij} (i.e., the maximum depth of that core divided by the number of density measurements). Due to increased averaging, we expect smoother snow density curves with longer $dx_{\mathbf{s}_{ij}}$. The core lengths for the EAP and SEAT campaigns are internally consistent in that, if $m(\mathbf{s}_{ij}) = m(\mathbf{s}_{i'j'})$, $dx_{\mathbf{s}_{ij}} = dx_{\mathbf{s}_{i'j'}}$. The SDM and US-ITASE expeditions do not use the same core lengths $dx_{\mathbf{s}_{ij}}$ to measure density for each core, an issue we address through a heteroscedastic error model. Most density measurements were taken in the field, which, unsurprisingly, poses several challenges. Many of the cores display anomalous density measurements that are likely erroneous, motivating the use of error distributions that down-weight these anomalies. Altogether, these data attributes motivate using an error model with heavy tails, random effects to account for research group differences, and weighting that accounts for differences in the core length used to measure snow density.

In Figure 1, we plot the locations of the cores, the number of density measurements from each core, maximum depth of the core, and the observed density measurements as a function

of depth for each site. Although snow density cannot exceed ρ_I , some measurements violate this limit, suggesting that our model for $y(\mathbf{s}_{ij}, x)$ must permit values greater than ρ_I , while a reasonable model for the mean function should constrain it between $(0, \rho_I]$.

As discussed, the HL model uses surface mass balance ($\text{SMB}(\mathbf{s})$) and the average temperature 10-m below the surface ($T(\mathbf{s})$). We have access to a dataset of temperature 10-m below the surface (Bohlander & Scambos, 2001) and the ERA-Interim 2-m air temperature data averaged from 1979 to 2014 (Molteni et al., 1996), which we call $T_{(2)}(\mathbf{s})$ to distinguish it from $T(\mathbf{s})$. Because the ERA-Interim 2-m air temperature data is very coarse, we use a smoothed temperature surface (White et al., 2019). In Figure 3, we plot the 2-m air temperature, observed temperature 10-m below the surface, and a scatterplot of these temperatures with a least-square regression line.

The average 2-m air temperature is higher than the temperature below the surface, and the relationship between the two temperatures appears to be linear with some heteroscedasticity. The simple linear regression model has an $R^2 = 0.923$. Although there is relatively little variability in temperature 10-m below not explained by 2-m air temperature, there is also spatial autocorrelation in the residuals for temperature 10-m below the surface given 2-m air temperature. Thus, we use a simple spatially-varying intercept model to estimate $T(\mathbf{s})$ at the 56 unique core locations and use its posterior mean for the HL model and our extensions. We use the posterior mean SMB from White et al. (2019) who use a spatial generalized linear model to interpolate $\text{SMB}(\mathbf{s})$. The posterior means of $T(\mathbf{s})$ and $\text{SMB}(\mathbf{s})$ are plotted in Figure 3. While we could model density, temperature, and SMB jointly, joint modeling poses significant computational challenges.

Using the posterior means for $T(\mathbf{s})$ and $\text{SMB}(\mathbf{s})$, plotted in Figure 3, we compare the HL model fit for each core to the observed field data. While the model matches the overall trend of density in general, it fails to accurately estimate snow density in many cases. To illustrate, we plot the fit of the HL model for two SDM cores (cores 4 and 8), one SEAT core (core 13), and one US-ITASE cores (core 49) in Figure 2. The HL model fit is generally good for core 4, undershoots the observed values for core 8, overshoots density measurements for much of core 12, and under- and over-estimates densities in core 49. These model failures suggest that a single HL model for all cores is inappropriate and that the model should vary site-to-site. We revisit the fits of our proposed models for these same cores in Section 4.3.

We fit piecewise linear models with the same discontinuities as the HL model to explore

whether there are evident spatial patterns in HL model fits. We fit these models on the logit-transformed density measurements less than ρ_I at each core. For each coefficient, we plot the binned semivariogram with the fit for an exponential semivariogram in Figure 4 to explore spatial patterns in the estimated regression coefficients. These show spatial patterns motivating a spatial model for the parameters of the HL model.

3 Spatially-Varying Snow Density Models

3.1 Spatially-Varying Snow Density Model

Motivated by the systematic errors in the HL model (Figure 2) and the spatial autocorrelation of parameters in Figure 4, we propose a joint hierarchical spatial model for the HL model parameters for each stage of our model and the critical densities ρ_1 , ρ_2 , and ρ_3 . We call this the spatially-varying snow density (SVSD) model. In the SVSD model, we denote the spatially-varying densification rates for each stage of the SVSD model, indexed with the subscript $l = 1, 2, 3, 4$, as $A_l(\mathbf{s})$, $E_l(\mathbf{s})$, where each stage is separated by critical densities $\rho_1(\mathbf{s})$, $\rho_2(\mathbf{s})$, and $\rho_3(\mathbf{s})$.

We specify a joint spatial process for parameters $\alpha(\mathbf{s})$, $A_l(\mathbf{s})$, $E_l(\mathbf{s})$, $\rho_1(\mathbf{s})$, $\rho_2(\mathbf{s})$, and $\rho_3(\mathbf{s})$. We model $\alpha(\mathbf{s})$ using a Gaussian (spatial) process. Because $A_l(\mathbf{s})$ and $E_l(\mathbf{s})$ are positive, we model these parameters on the log scale. Similarly, we use generalized logistic transformations of $\rho_1(\mathbf{s})$, $\rho_2(\mathbf{s})$, and $\rho_3(\mathbf{s})$ to bound these quantities to physically-plausible quantities, between (0.42-0.68), (0.68-0.78), and (0.78-0.88) g/cm³, respectively. Moreover, because each stage of our model only has one rate, we use a spatial prior distribution that enables information sharing between sites to make $A_l(\mathbf{s})$ and $E_l(\mathbf{s})$ jointly identifiable. Importantly, the SVSD model allows us to estimate how thermal processes vary over space.

Since snow density is bounded between $(0, \rho_I]$, we specify our mean function $\mu(\mathbf{s}, x)$, rather than the observations, in terms of the SVSD model. We write this as

$$\log \left(\frac{\mu(\mathbf{s}, x)}{\rho_I - \mu(\mathbf{s}, x)} \right) = \alpha(\mathbf{s}) + \mathbf{z}_\theta(\mathbf{s}, x)^T \mathbf{k}(\mathbf{s}_i), \quad (6)$$

where $\mathbf{z}_\theta(\mathbf{s}, x)$ and $\mathbf{k}(\mathbf{s})$ are made up of elements

$$\begin{aligned}
z_1(\mathbf{s}, x) &= \rho_I \min(x, \kappa_1(\mathbf{s})), & k_1(\mathbf{s}) &= A_1(\mathbf{s}) \exp\left(-\frac{E_1(\mathbf{s})}{RT(\mathbf{s})}\right) \\
z_2(\mathbf{s}, x) &= \frac{\rho_I \min(x - \kappa_1(\mathbf{s}), \kappa_2(\mathbf{s}) - \kappa_1(\mathbf{s}))}{\sqrt{SMB(\mathbf{s})}} \mathbf{1}(x > \kappa_1(\mathbf{s})), & k_2(\mathbf{s}) &= A_2(\mathbf{s}) \exp\left(-\frac{E_2(\mathbf{s})}{RT(\mathbf{s})}\right) \\
z_3(\mathbf{s}, x) &= \frac{\rho_I \min(x - \kappa_2(\mathbf{s}), \kappa_3(\mathbf{s}) - \kappa_2(\mathbf{s}))}{\sqrt{SMB(\mathbf{s})}} \mathbf{1}(x > \kappa_2(\mathbf{s})), & k_3(\mathbf{s}) &= A_3(\mathbf{s}) \exp\left(-\frac{E_3(\mathbf{s})}{RT(\mathbf{s})}\right) \\
z_4(\mathbf{s}, x) &= \frac{\rho_I (x - \kappa_3(\mathbf{s}))}{\sqrt{SMB(\mathbf{s})}} \mathbf{1}(x > \kappa_3(\mathbf{s})). & k_4(\mathbf{s}) &= A_4(\mathbf{s}) \exp\left(-\frac{E_4(\mathbf{s})}{RT(\mathbf{s})}\right)
\end{aligned}$$

Because they are parameter dependent, we write the space-depth covariates as $\mathbf{z}_\theta(\mathbf{s}, x)$. Although we do not model the depth change points $\kappa_1(\mathbf{s})$, $\kappa_2(\mathbf{s})$, and $\kappa_3(\mathbf{s})$ directly, we infer them from the critical densities $\rho_1(\mathbf{s})$, $\rho_2(\mathbf{s})$, and $\rho_3(\mathbf{s})$, as in (4).

Somewhat as an aside, this model can be scaled to be expressed as a generalized linear I-spline model with unknown knots, where the critical depths $\kappa_1(\mathbf{s})$, $\kappa_2(\mathbf{s})$, and $\kappa_3(\mathbf{s})$ are equivalent to interior knots of the I-spline. I-splines are defined as the integral of M-spline, or, equivalently, as the integral of a scaled B-spline (see Ramsay, 1988; Meyer, 2008, for more details). White et al. (2020) use M-spline basis functions to construct integrated spatial processes for monotone function estimation.

3.2 Functionally-Smoothed Snow Density Model

Because the HL model is piecewise linear (on the transformed scale) and could thus miss important deviations from linearity, we present the functionally-smoothed SVSD model. Because parameter inference is our primary goal, we constrain the smooth component of this model to lie in the orthogonal columns space of $\mathbf{z}_\theta(\mathbf{s}, x)$ for each core. If parameter inference is the only goal, then this extension may be unnecessary. However, if snow density prediction is of interest, this extension may boost the model's predictive power, depending on the dataset.

Because we orthogonalize the smooth component of the smoothed SVSD model with respect to $\mathbf{z}_\theta(\mathbf{s}, x)$ at observed depths, let $\mathbf{Z}(\mathbf{s}_{ij})$ be a matrix with $\mathbf{z}_\theta(\mathbf{s}_{ij}, x)$ at all measured depths for core \mathbf{s}_{ij} , and define the projection into the orthogonal columns space of $\mathbf{Z}(\mathbf{s}_{ij})$ as

$$P_z^\perp(\mathbf{s}_{ij}) = \mathbf{I} - \mathbf{Z}(\mathbf{s}_{ij}) (\mathbf{Z}(\mathbf{s}_{ij})^T \mathbf{Z}(\mathbf{s}_{ij}))^{-1} \mathbf{Z}(\mathbf{s}_{ij})^T.$$

Note that we do not include a column of ones in $\mathbf{Z}(\mathbf{s}_{ij})$ because we wish to preserve the simple correspondence between $\alpha(\mathbf{s})$ and the expected snow density at the surface (i.e., $x = 0$).

If we let $\mathbf{h}_\theta^\perp(\mathbf{s}_{ij}, x) = P_z^\perp(\mathbf{s}_{ij})\mathbf{h}(x)$, where $\mathbf{h}(x)$ are covariates specified through basis functions of smooth curves (e.g., polynomial splines), then the smoothed SVSD model is

$$\log\left(\frac{\mu(\mathbf{s}_{ij}, x)}{\rho_I - \mu(\mathbf{s}_{ij}, x)}\right) = \alpha(\mathbf{s}) + \mathbf{z}_\theta(\mathbf{s}_{ij}, x)^T \mathbf{k}(\mathbf{s}) + \mathbf{h}_\theta^\perp(\mathbf{s}_{ij}, x)^T \boldsymbol{\beta}(\mathbf{s}), \quad (7)$$

where $\boldsymbol{\beta}(\mathbf{s})$ are corresponding spatially-varying mean-zero coefficients. We write this model in terms of $\mu(\mathbf{s}_{ij})$ rather than $\mu(\mathbf{s})$ because the projection is dependent on depths measured at core \mathbf{s}_{ij} . The parameters, however, still only depend on location \mathbf{s} . The smoothed SVSD model preserves inference on Arrhenius parameters but is more flexible, allowing deviations from piecewise linearity. Of course, $\mathbf{h}_\theta^\perp(\mathbf{s}_{ij}, x)^T \boldsymbol{\beta}(\mathbf{s})$ could be replaced with a mean-zero Gaussian random effect with covariance \mathbf{S} augmented as $P_z^\perp(\mathbf{s}_{ij})\mathbf{S}P_z^\perp(\mathbf{s}_{ij})^T$, but, given the relatively simple shape of these data and the number of measurements, we use polynomials and splines instead of Gaussian processes.

4 Methods and Models

4.1 Models Comparison

In our model comparison, we address four modeling questions: (1) Which truncated error distribution best suits these data? (2) How should we account for group differences in measurement accuracy, including the core length used to obtain density measurements? (3) Which cross-covariance model is best for our spatially-varying HL model? (4) Should our model include deviations from the piecewise linearity by including *smoother* components to the model?

We use the Watanabe–Akaike information criterion (WAIC) as our model selection criterion (Watanabe, 2010), computed using each observation as a partition (Vehtari et al., 2017). We use WAIC in favor of deviance information criterion (DIC) (Spiegelhalter et al., 2002) because WAIC is a generally more stable approximation to cross-validation than DIC, uses the entire posterior distribution, and is less prone to select overfit models.

We discuss model comparison results in detail in Appendix A. To summarize the results, we find that using a truncated t -distribution is better than the corresponding truncated

Normal models. Error distributions with hierarchically-specified scale parameters, weighted to account for the length of the core used to obtain density measurements, improve WAIC relative to homoscedastic models. We select a separable cross-covariance model for the spatially-varying HL parameters because it has the lowest WAIC, but we did not find significant differences in model performance for most cross-covariance specifications. Lastly, we compare seven possible functional smoothings for the smoothed SVSD and select a quadratic spline with three knots to specify (7) because it has the lowest WAIC; however, several spline models perform comparably. We present our final model in Section 4.2.

4.2 Hierarchical Model

Using the quantities defined in Sections 2 and 3.2, our hierarchical model is

$$\begin{aligned}
 y(\mathbf{s}_{ij}, x) &\sim t_\nu \left(\mu(\mathbf{s}_{ij}, x), \tau_{\mathbf{s}_{ij}}^2, 0, \infty \right) \\
 \log \left(\frac{\mu(\mathbf{s}_{ij}, x)}{\rho_I - \mu(\mathbf{s}_{ij}, x)} \right) &= \alpha(\mathbf{s}) + \mathbf{z}_\theta(\mathbf{s}, x)^T \mathbf{k}(\mathbf{s}) + \mathbf{h}_\theta^\perp(\mathbf{s}_{ij}, x)^T \boldsymbol{\beta}(\mathbf{s}) \\
 \log(\tau_{\mathbf{s}_{ij}}^2) &\sim \mathcal{N} \left\{ \log \left[\tau_{m(\mathbf{s}_{ij})}^2 dx_{\mathbf{s}_{ij}}^{\eta_{m(\mathbf{s}_{ij})}} \right], \sigma_\tau^2 \right\},
 \end{aligned} \tag{8}$$

where $t_\nu(\mu(\mathbf{s}_{ij}, x), \tau_{\mathbf{s}_{ij}}^2, 0, \infty)$ is a t -distribution, truncated below by 0, with location $\mu(\mathbf{s}_{ij}, x)$ and scale $\tau_{\mathbf{s}_{ij}}$. We use the truncated- t distribution to give a coherent model, but the truncation has little practical effect on our analysis because snow densities are not close to zero. As a consequence, $\mu(\mathbf{s}, x)$ is effectively a mean function rather than only a location function. For the EAP and SEAT campaigns, there is no variation in $dx_{\mathbf{s}_{ij}}$; therefore, we fix $\eta_{m(\mathbf{s}_{ij})} = 0$ because this weighting parameter is not identifiable.

As discussed, we specify a joint spatial process for the smoothed SVSD model through a multivariate Gaussian process (MGP) model for the intercept, transformed Arrhenius constant parameters, and critical densities. We let $\boldsymbol{\theta}(\mathbf{s})$ be transformed spatial parameters, $\alpha(\mathbf{s})$, $\log(A_1(\mathbf{s}))$, $\log(A_2(\mathbf{s}))$, $\log(A_3(\mathbf{s}))$, $\log(A_4(\mathbf{s}))$, $\log(E_1(\mathbf{s}))$, $\log(E_2(\mathbf{s}))$, $\log(E_3(\mathbf{s}))$, $\log(E_4(\mathbf{s}))$, $\log\left(\frac{\rho_1(\mathbf{s})-0.42}{0.68-\rho_1(\mathbf{s})}\right)$, $\log\left(\frac{\rho_2(\mathbf{s})-0.68}{0.78-\rho_2(\mathbf{s})}\right)$, and $\log\left(\frac{\rho_3(\mathbf{s})-0.78}{0.88-\rho_3(\mathbf{s})}\right)$, and we specify $\boldsymbol{\theta}(\mathbf{s})$ using a multivariate GP. Thus, the transformed spatial parameters at observed sites $\boldsymbol{\theta}(\mathcal{S}) = (\boldsymbol{\theta}(\mathbf{s}_1)^T, \dots, \boldsymbol{\theta}(\mathbf{s}_{n_s})^T)^T$ follows a multivariate-normal distribution. That is,

$$\boldsymbol{\theta}(\mathcal{S}) \sim \mathcal{N}(\mathbf{M}\boldsymbol{\gamma}, \mathbf{R} \otimes \mathbf{V}), \tag{9}$$

where the hierarchical mean for $\boldsymbol{\theta}(\mathbf{s})$ is

$$\mathbf{M}\boldsymbol{\gamma} = (\gamma_\alpha, \gamma_{A_1}, \gamma_{A_2}, \gamma_{A_2}, \gamma_{A_2}, \gamma_{E_1}, \gamma_{E_2}, \gamma_{E_2}, \gamma_{E_2}, \gamma_{\rho_1}, \gamma_{\rho_2}, \gamma_{\rho_3})^T,$$

$\boldsymbol{\gamma} = (\gamma_\alpha, \gamma_{A_1}, \gamma_{A_2}, \gamma_{E_1}, \gamma_{E_2}, \gamma_{\rho_1}, \gamma_{\rho_2}, \gamma_{\rho_3})^T$, and \mathbf{M} is a 12×8 matrix that repeats elements of $\boldsymbol{\gamma}$ to account for the weak transitions suggested by Hörhold et al. (2011). We use repeated elements in our hierarchical mean because densification rates show little or weak transitions at the second and third critical densities (Hörhold et al., 2011). The i th row and i' th column of the correlation matrix \mathbf{R} is $\exp(\phi d(\mathbf{s}_i, \mathbf{s}_{i'}))$.

For the spatial-varying coefficients $\beta_k(\mathbf{s})$ of the orthogonalized spline basis functions, we assume that

$$\beta_k(\mathcal{S}) \sim \mathcal{N}(0, \sigma_{\beta_m}^2 \mathbf{R}_\beta), \quad (10)$$

where the i th row and i' th column of the correlation matrix $(\mathbf{R})_{i,i'} = \exp(-\phi_\beta d(\mathbf{s}_i, \mathbf{s}_{i'}))$. Therefore, we assume that the spatially-varying spline coefficients are centered on zero, share a common decay parameter, but have their own scale parameter.

4.3 Prior Distributions, Model Fitting, and Prediction

We use the following prior distributions for our hierarchical model:

$$\begin{array}{lll} \gamma_\alpha \sim \mathcal{N}(-0.5, 0.5^2) & \gamma_{\rho_1} \sim \mathcal{N}(0, 1) & \sigma_\tau^2 \sim \mathcal{IG}(2.1, 1/10) \\ \gamma_{A_1} \sim \mathcal{N}(2.4, 0.2^2) & \gamma_{\rho_2} \sim \mathcal{N}(0, 1) & \mathbf{V} \sim \text{Inverse-Wishart}(13, \mathbf{I}) \\ \gamma_{A_2} \sim \mathcal{N}(6.35, 0.2^2) & \gamma_{\rho_3} \sim \mathcal{N}(0, 1) & \phi^{-1} \sim \text{Unif}(10, 1000) \\ \gamma_{E_1} \sim \mathcal{N}(9.23, 0.2^2) & \nu \sim \text{Unif}(4, 30) & \sigma_{\beta_k}^2 \sim \mathcal{IG}(2.1, 1/10) \\ \gamma_{E_2} \sim \mathcal{N}(9.97, 0.25^2) & \log(\tau_{m(\mathbf{s}_{ij})}^2) \sim \mathcal{N}(-7, 4) & \phi_\beta^{-1} \sim \text{Unif}(10, 1000) \\ & \eta_{m(\mathbf{s}_{ij})} \sim \mathcal{N}(-8, 4) & \end{array} \quad (11)$$

The hierarchical mean parameters are informative, and we use the parameters from the original HL parameters in Herron & Langway (1980) to specify posterior medians. Because the t -distribution is nearly Gaussian when $\nu \geq 30$, we set 30 degrees of freedom as the upper bound. We set the lower bound on ν to be four so that the first four moments of the error distribution are finite. The prior median for $\log(\tau_{m(\mathbf{s}_{ij})}^2)$ corresponds to a median

standard deviation of about 0.03 (for large ν) but allows much larger and smaller values. We choose this because, for a fixed depth, observations are quite concentrated about the center of the density curve. Because we do not know how much values of $\log(\tau_{\mathbf{s}_{ij}}^2)$ may vary, we use a somewhat diffuse prior distribution on σ_τ^2 . We choose the prior distribution for $\eta_{m(\mathbf{s}_{ij})}$ because using more of the core to obtain a density measurement yields a smoother curve (i.e., less variance).

We use uniform prior distributions for the range parameters of our spatially-varying HL parameters ϕ^{-1} and cubic spline coefficients ϕ_β^{-1} . For the exponential correlation function, our prior distribution bounds the effective range of our spatially-varying parameters between 30 and 3,000 km. Because we expect the spatially-varying parameters of our model not to differ much from the hierarchical means, we use flexible prior distributions for \mathbf{V} and $\sigma_{\beta_k}^2$ that heavily weight small values. For exponential covariance models, only the product of scale and decay parameters is identifiable, and model-based interpolations are equal if the product of scale and decay parameters is equal (Zhang, 2004). Thus, we are not able to make good inference on ϕ , ϕ_β , \mathbf{V} , on $\sigma_{\beta_k}^2$ individually.

We use an adaptive Markov chain Monte Carlo (MCMC) model fitting approach to obtain posterior samples using Metropolis-within-Gibbs and Gibbs updates. We sample HL parameters $\theta(\mathbf{s})$ site-wise using the multivariate Metropolis algorithm with multivariate Normal proposal distributions centered on the current parameter values and covariance equal to the scaled empirical covariance of the site-specific parameters (Haario et al., 2001). We use the univariate Metropolis algorithm updates with Normal random walk proposal distributions to sample from the posterior distributions of $\beta_k(\mathbf{s})$ and ν , while we use the univariate Metropolis-Hastings algorithm with log-Normal random walk proposal distributions to sample from the posterior distributions of $\tau^2(\mathbf{s}_{ij})$, ϕ , and ϕ_β . During the burn-in part of our MCMC, we tune the candidate variances so that acceptance rates are between 0.2-0.6 for univariate updates and 0.15-0.5 for multivariate updates. Because spatially-varying parameters mix slowly due to high correlation, we follow the recommendation of Neal (1998), updating the spatially-varying parameters several times, five, in this case, each iteration of the sampler. Because posterior conditional distributions for γ , $\log(\tau_{m(\mathbf{s}_{ij})}^2)$, $\eta_{m(\mathbf{s}_{ij})}$, σ_τ^2 , and $\sigma_{\beta_k}^2$ can be found in closed form, we update these parameters using Gibbs updates.

Using our model, we can estimate model parameters and mean density curves. Our primary goal is estimating how various parameters (or functions of parameters) vary spa-

tially. To estimate spatially-varying parameters at new locations \mathbf{s}_{new} , we simply sample the transformed parameters $\boldsymbol{\theta}(\mathbf{s}_{new})$ using the appropriate conditional normal distribution. If estimating the mean $\mu(\mathbf{s}, x)$ or observed density $y(\mathbf{s}, x)$ at a location outside of \mathcal{S} , then we follow the same process for interpolating regression spline coefficients as we use for spatially-varying HL parameters and use composition sampling to sample from the posterior predictive distribution (Tanner, 1996).

5 Results

We run our MCMC model fitting for 250,000 iterations, discard the first 50,000, and keep every 20th sample. Our results are based on the remaining 10,000 posterior samples. Before presenting results, we again emphasize that the truncated- t distribution gives a coherent model, but the truncation has no practical effect on our analysis because snow densities are not close to zero. For this reason, the location function $\mu(\mathbf{s}, x)$ is essentially a mean function.

5.1 Hierarchical Summaries

In this subsection, we present the posterior summaries of the hierarchical parameters and compare the hierarchical mean to the parameter estimates of the HL model, as well as other scientific assertions about snow densification (Revisit Section 2.1 for this discussion). We defer discussion of several parameters to Appendix B. We present posterior summaries (posterior mean, median, standard deviation, and a 90% central credible interval) in Table 1. To compare previous parameter estimates to our posterior distribution, we calculate the quantile of our posterior distribution corresponding to the previous estimates (See Table 1).

Parameter estimates from the original HL model correspond to quantiles between (0.365 and 0.756). The first critical density suggested by Herron & Langway (1980), 0.55 g/cm³, corresponds to the 84% of our posterior distribution, suggesting that the snow cores in our dataset suggest a lower critical density than that in Herron & Langway (1980). As discussed in Hörhold et al. (2011), several studies suggest critical densities at 0.73 and 0.83 g/cm³, which are, respectively, the 0.27 and 0.07 quantile of the posterior distribution. Although the hierarchical mean of our smoothed SVSD model is compatible with previous scientific estimates for snow densification, a global model for snow densification fails to accurately capture site-specific density patterns. We explore how these patterns change over space in

Section 5.2.

In Figure 5, we give violin plots of the posterior distributions for the core-specific scale parameters $\sqrt{\tau_{\mathbf{s}_{ij}}^2}$. Recall that $\log(\tau_{\mathbf{s}_{ij}}^2)$ are hierarchically-specified and factor in expedition-specific scale and weighting parameters to account for the length of the core used to obtain density measurements, as well as campaign-specific differences. The differences between expeditions are apparent in Figure 5. EAP snowpits and SEAT cores generally have shorter averaging lengths $dx_{\mathbf{s}_{ij}}$; thus, unsurprisingly, EAP snowpits have the highest estimated standard deviation, followed by SEAT cores. SDM and US-ITASE cores have smaller estimated standard deviations, on average, but the US-ITASE cores show high variability in standard deviation.

5.2 Spatially-Varying Parameters

In this section, we focus on the spatially-varying component of our model. Specifically, we interpolate all spatially-varying HL parameters on a grid of about 2500 points over the convex hull of our data. Importantly, the model’s Arrhenius constants depend on temperature 10-m below the surface. We rely on model-based spatial interpolations presented in Section 2 to estimate $T(\mathbf{s})$ which, together with $A_l(\mathbf{s})$, $E_l(\mathbf{s})$, define the Arrhenius constant for the l th stage of densification.

In Figure 6, we plot the posterior median of surface density, three critical densities, and the Arrhenius constants and parameters for the first two densification stages. We use the median because the untransformed parameters have some extreme values. In each plot, we plot the location of observations and note that the uncertainty in our estimates increases as the distance to observations increases. Altogether, these plots show high heterogeneity in the spatially-varying parameters. We give measures of uncertainty for all spatially-varying parameters in Appendix B. From these uncertainty plots, we see the trends we would expect using a spatial model: uncertainty is higher (i) as the distance to observations increases and (ii) at the boundary of where our data is.

We follow-up on the assertion that stages two, three, and four are not significantly different (Hörhold et al., 2011) which we assume is true in the mean of the hierarchical model. To do this, we compute and plot the posterior probability that $k_2(\mathbf{s}) > k_3(\mathbf{s})$, $k_2(\mathbf{s}) > k_4(\mathbf{s})$, and $k_3(\mathbf{s}) > k_4(\mathbf{s})$ in Figure 7. In general, the estimated differences appear to be somewhat weak, confirming the suggestion of weak transitions between densification stages at many

sites [Hörhold et al. \(2011\)](#). However, there appear to be some regions where the densification rates differ across the last three stages of our model.

5.3 Comparison of Snow Density Estimates

To highlight the differences between the original HL model (3), the SVSD model (6), and the smoothed SVSD model (7), we revisit the cores discussed in Section 2.2 and plotted in Figure 2. For these four cores, we plot the three model fits in Figure 8. For all cores, there is a clear improvement using both of our proposed models. However, the smoothed SVSD model is only apparently better for some cores. For the two SDM cores, 4 and 8, there is no evident improvement using the more complicated smoothed SVSD model. For core 12, the smoothed SVSD model is much better than the SVSD model, while it is only slightly better for core 49. Overall, we find that the smoothed SVSD model was best for data-rich cores and provided only marginal improvement for cores with relatively fewer measurements.

6 Conclusions and Future Work

We analyzed a dataset of 14,844 density measurements taken from 57 snow cores drilled at 56 sites in West Antarctica using a novel model that preserves inference on the physical constants while incorporating spatial and functional smoothing. Our model allowed us to explore how important physical quantities vary over West Antarctica. Using this model, we explored how estimated snow densification patterns change over space and compared our model to previous studies.

The proposed model provides important contributions to the polar and ice sheet research communities. Perhaps most importantly, the model performs spatial modeling of snow densification rate constants, allowing for improved inference on the regional variability of physical constants. Specifically, this modeling includes flexibility in the densification rates and density/depth cutoffs between different stages of densification, better capturing the true variability in such parameters. The model also allows for non-linear deviations in densification rate parameters and is thus able to better handle noisy data, either from measurement errors or physical disequilibrium effects. Finally, our model includes quantitative bounds of estimate uncertainty. All of these attributes are valuable for the scientific community, while most current observation-based snow density models include few if any of the above points.

The proposed model, therefore, represents an important step forward in providing spatially-distributed and error-constrained estimates of density with depth in Antarctic snow from *in-situ* data.

This research opens several paths to further advance the state of polar cryospheric science. Several areas of the discipline rely on spatially-distributed estimates of snow density with depth. The proposed density modeling framework should be immediately applicable to estimates of annual surface mass balance using radar data, which require snow density as input (Keeler et al., 2020). Additionally, recent investigations of Antarctica increasingly rely on the outputs of coupled climate models and climate reanalyses to investigate SMB, mass loss, and similar climate changes (see, e.g. Lenaerts et al., 2012; Wessem et al., 2018). The improved prediction of snow/ice densities from the results of this study can provide context for these climate models and help to assess their performance for regions across West Antarctica. Finally, due to the large commitment and expense required for *in-situ* data collection in Antarctica, the careful selection of ice/snow coring sites is essential for expedition planning and execution. We, therefore, plan to pursue a follow-up project proposing a spatial design method for selecting where and how deep cores should be drilled. As more data become available, we speculate that richer spatial models may be beneficial. More recently, snow cores are measured using high-resolution approaches that yield $\approx 50,000$ density measurements per core. With such cores, smoothed HL models become computationally prohibitive; thus, we suggest exploring appropriate approximations for this framework. Future extensions could also explore stochastic differential equation models for snow density.

Beyond applications to Antarctica, the proposed extensions to snow density modeling should be immediately applicable to other glaciated regions (e.g. the Greenland Ice Sheet, Andean ice caps, High Mountain Asia, etc.). All of these regions are uniquely vulnerable to ongoing climate changes and represent critical research targets for the cryospheric community. Likewise, the proposed framework for piecewise linear modeling is applicable generally to a myriad of similar problems. Predictions and interpolations of spatially-varying parameters are ubiquitous in Earth and environmental sciences, with piecewise-linear models common in many applications. Examples are as varied as climate reconstructions from tree rings (Schofield et al., 2016), trend analysis in ocean and climate data (Banesh et al., 2019), precipitation effects on biogeochemical cycles (Wang et al., 2017), quantifying environmental impacts on economies (Engle et al., 1986; Du et al., 2017), and estimating effects of climate

change on food production (Katz, 1977; Tebaldi & Lobell, 2008; Ortiz-Bobea & Tack, 2018). Application of the proposed modeling framework could improve predictions and inference in many fields with models similarly utilizing piecewise linear components.

References

- Albert, M., Shuman, C., Courville, Z., Bauer, R., Fahnestock, M., & Scambos, T. (2004). Extreme firn metamorphism: Impact of decades of vapor transport on near-surface firn at a low-accumulation glazed site on the East Antarctic plateau. *Annals of Glaciology*, *39*, 73–78.
- Alley, R. B., Bolzan, J. F., & Whillans, I. M. (1982). Polar firn densification and grain growth. *Annals of Glaciology*, *3*, 7–11.
- Álvarez, M. A., & Lawrence, N. D. (2011). Computationally efficient convolved multiple output Gaussian processes. *Journal of Machine Learning Research*, *12*(May), 1459–1500.
- Arthern, R. J., Vaughan, D. G., Rankin, A. M., Mulvaney, R., & Thomas, E. R. (2010). In situ measurements of Antarctic snow compaction compared with predictions of models. *Journal of Geophysical Research: Earth Surface*, *115*(F3). Retrieved 2020-06-05, from <https://agupubs.onlinelibrary.wiley.com/doi/abs/10.1029/2009JF001306> (eprint: <https://agupubs.onlinelibrary.wiley.com/doi/pdf/10.1029/2009JF001306>) doi: 10.1029/2009JF001306
- Banerjee, S., Carlin, B. P., & Gelfand, A. E. (2014). *Hierarchical modeling and analysis for spatial data*. CRC press.
- Banesh, D., Petersen, M., Wendelberger, J., Ahrens, J., & Hamann, B. (2019, October). Comparison of piecewise linear change point detection with traditional analytical methods for ocean and climate data. *Environmental Earth Sciences*, *78*(21), 623. Retrieved 2020-09-02, from <https://doi.org/10.1007/s12665-019-8636-y> doi: 10.1007/s12665-019-8636-y
- Bohlander, J., & Scambos, T. (2001). Thermap Antarctic ice sheet temperature data. *Boulder, CO: National Snow and Ice Data Centre*.

- Burgener, L., Rupper, S., Koenig, L., Forster, R., Christensen, W. F., Williams, J., . . . Riley, L. (2013, May). An observed negative trend in West Antarctic accumulation rates from 1975 to 2010: Evidence from new observed and simulated records. *Journal of Geophysical Research-Atmospheres*, *118*(10), 4205–4216.
- Chen, T., de Jeu, R. A. M., Liu, Y. Y., van der Werf, G. R., & Dolman, A. J. (2014, January). Using satellite based soil moisture to quantify the water driven variability in NDVI: A case study over mainland Australia. *Remote Sensing of Environment*, *140*, 330–338. Retrieved 2020-09-02, from <http://www.sciencedirect.com/science/article/pii/S0034425713002800> doi: 10.1016/j.rse.2013.08.022
- Csatho, B. M., Schenk, A. F., Veen, C. J. v. d., Babonis, G., Duncan, K., Rezvanbehbahani, S., . . . Angelen, J. H. v. (2014, December). Laser altimetry reveals complex pattern of Greenland Ice Sheet dynamics. *Proceedings of the National Academy of Sciences*, *111*(52), 18478–18483. Retrieved 2020-09-17, from <https://www.pnas.org/content/111/52/18478> (Publisher: National Academy of Sciences Section: Physical Sciences) doi: 10.1073/pnas.1411680112
- Dai, L., Zhou, J., Chen, L., Huang, K., Wang, Q., & Zha, G. (2019). Flood-risk analysis based on a stochastic differential equation method. *Journal of Flood Risk Management*, *12*(S1), e12515. Retrieved 2020-09-02, from <https://onlinelibrary.wiley.com/doi/abs/10.1111/jfr3.12515> (eprint: <https://onlinelibrary.wiley.com/doi/pdf/10.1111/jfr3.12515>) doi: 10.1111/jfr3.12515
- Das Bhowmik, R., Seo, S. B., & Sahoo, S. (2018). Streamflow simulation using bayesian regression with multivariate linear spline to estimate future changes. *Water*, *10*(7), 875.
- Du, D., Zhao, X., & Huang, R. (2017). The impact of climate change on developed economies. *Economics Letters*, *153*, 43–46.
- Eisen, O., Frezzotti, M., Genthon, C., Isaksson, E., Magand, O., van den Broeke, M. R., . . . Vaughan, D. G. (2008, April). Ground-based measurements of spatial and temporal variability of snow accumulation in East Antarctica. *Reviews of Geophysics*, *46*(1), RG2001. (WOS:000255079700001) doi: 10.1029/2006RG000218

- Engle, R. F., Granger, C. W., Rice, J., & Weiss, A. (1986). Semiparametric estimates of the relation between weather and electricity sales. *Journal of the American statistical Association*, *81*(394), 310–320.
- Freitag, J., Wilhelms, F., & Kipfstuhl, S. (2004). Microstructure-dependent densification of polar firn derived from x-ray microtomography. *Journal of Glaciology*, *50*(169), 243–250.
- Gelfand, A. E., Kim, H.-J., Sirmans, C., & Banerjee, S. (2003). Spatial modeling with spatially varying coefficient processes. *Journal of the American Statistical Association*, *98*(462), 387–396.
- Genton, M. G., & Kleiber, W. (2015). Cross-covariance functions for multivariate geostatistics. *Statistical Science*, 147–163.
- Gneiting, T., Kleiber, W., & Schlather, M. (2010). Matérn cross-covariance functions for multivariate random fields. *Journal of the American Statistical Association*, *105*(491), 1167–1177.
- Gow, A. J. (1975). Time-temperature dependence of sintering in perennial isothermal snowpacks. *International Association of Hydrological Sciences Publications*, *114*, 25–41.
- Grzebyk, M., & Wackernagel, H. (1994). Multivariate analysis and spatial/temporal scales: real and complex models. In *Proceedings of the xviiith international biometrics conference* (Vol. 1, pp. 19–33).
- Haario, H., Saksman, E., & Tamminen, J. (2001). An adaptive Metropolis algorithm. *Bernoulli*, *7*(2), 223–242.
- Heckman, N. E. (1986). Spline smoothing in a partly linear model. *Journal of the Royal Statistical Society: Series B (Methodological)*, *48*(2), 244–248.
- Helsen, M. M., Broeke, M. R. v. d., Wal, R. S. W. v. d., Berg, W. J. v. d., Meijgaard, E. v., Davis, C. H., ... Goodwin, I. (2008, June). Elevation Changes in Antarctica Mainly Determined by Accumulation Variability. *Science*, *320*(5883), 1626–1629. Retrieved 2020-06-05, from <https://science.sciencemag.org/content/320/5883/1626> (Publisher: American Association for the Advancement of Science Section: Report) doi: 10.1126/science.1153894

- Herron, M. M., & Langway, C. C. (1980). Firn densification: An empirical model. *Journal of Glaciology*, 25(93), 373–385.
- Hodges, J. S., & Reich, B. J. (2010). Adding spatially-correlated errors can mess up the fixed effect you love. *The American Statistician*, 64(4), 325–334.
- Hörhold, M. W., Kipfstuhl, S., Wilhelms, F., Freitag, J., & Frenzel, A. (2011). The densification of layered polar firn. *Journal of Geophysical Research: Earth Surface*, 116(F1).
- Horner, G. J., Baker, P. J., Mac Nally, R., Cunningham, S. C., Thomson, J. R., & Hamilton, F. (2009). Mortality of developing floodplain forests subjected to a drying climate and water extraction. *Global Change Biology*, 15(9), 2176–2186.
- Howarth, R., Swaney, D., Billen, G., Garnier, J., Hong, B., Humborg, C., ... Marino, R. (2012). Nitrogen fluxes from the landscape are controlled by net anthropogenic nitrogen inputs and by climate. *Frontiers in Ecology and the Environment*, 10(1), 37–43.
- Hughes, J., & Haran, M. (2013). Dimension reduction and alleviation of confounding for spatial generalized linear mixed models. *Journal of the Royal Statistical Society: Series B (Statistical Methodology)*, 75(1), 139–159.
- IPCC. (2013). *Climate Change 2013: The Physical Science Basis. Contribution of Working Group I to the Fifth Assessment Report of the Intergovernmental Panel on Climate Change*. Cambridge, United Kingdom and New York, NY, USA: Cambridge University Press.
- Johnson, J. B. (1998). A preliminary numerical investigation of the micromechanics of snow compaction. *Annals of Glaciology*, 26, 51–54.
- Katz, R. W. (1977). Assessing the impact of climatic change on food production. *Climatic Change*, 1(1), 85–96.
- Keeler, D. G., Rupper, S. B., Forster, R., & Miège, C. (2020). A Probabilistic Automated Isochrone Picking Routine to Derive Annual Surface Mass Balance From Radar Echograms. *IEEE Transactions on Geoscience and Remote Sensing*, 1–14. doi: 10.1109/TGRS.2020.2989102

- Kleiber, W., & Nychka, D. (2012). Nonstationary modeling for multivariate spatial processes. *Journal of Multivariate Analysis*, *112*, 76–91.
- Koenig, L. S., Ivanoff, A., Alexander, P. M., MacGregor, J. A., Fettweis, X., Panzer, B., ... Gogineni, P. (2016). Annual Greenland accumulation rates (2009-2012) from airborne snow radar. *Cryosphere*, *10*(4), 1739–1752. (WOS:000381218000016) doi: 10.5194/tc-10-1739-2016
- Koster, R. D., Schubert, S. D., DeAngelis, A. M., Molod, A. M., & Mahanama, S. P. (2020, August). Using a Simple Water Balance Framework to Quantify the Impact of Soil Moisture Initialization on Subseasonal Evapotranspiration and Air Temperature Forecasts. *Journal of Hydrometeorology*, *21*(8), 1705–1722. Retrieved 2020-09-02, from <https://journals.ametsoc.org/jhm/article/21/8/1705/348250/Using-a-Simple-Water-Balance> (Publisher: American Meteorological Society) doi: 10.1175/JHM-D-20-0007.1
- Lamorey, G., & Cooper, T. (2002). *Siple dome waiscores density data for shallow cores*. Retrieved from <https://nsidc.org/data/waiscores/density.html>
- Lenaerts, J. T. M., van den Broeke, M. R., van de Berg, W. J., van Meijgaard, E., & Munneke, P. K. (2012, February). A new, high-resolution surface mass balance map of Antarctica (1979-2010) based on regional atmospheric climate modeling. *Geophysical Research Letters*, *39*, L04501. (WOS:000300794400004) doi: 10.1029/2011GL050713
- Lewis, G., Osterberg, E., Hawley, R., Marshall, H. P., Meehan, T., Graeter, K., ... Ferris, D. (2019, November). Recent precipitation decrease across the western Greenland ice sheet percolation zone. *The Cryosphere*, *13*(11), 2797–2815. Retrieved 2020-02-25, from <https://www.the-cryosphere.net/13/2797/2019/> doi: <https://doi.org/10.5194/tc-13-2797-2019>
- Li, J., & Zwally, H. J. (2011). Modeling of firn compaction for estimating ice-sheet mass change from observed ice-sheet elevation change. *Annals of Glaciology*, *52*(59), 1–7.
- Maeno, N., & Ebinuma, T. (1983). Pressure sintering of ice and its implication to the densification of snow at polar glaciers and ice sheets. *The Journal of Physical Chemistry*, *87*(21), 4103–4110.

- Martinerie, P., Raynaud, D., Etheridge, D. M., Barnola, J.-M., & Mazaudier, D. (1992). Physical and climatic parameters which influence the air content in polar ice. *Earth and Planetary Science Letters*, *112*(1-4), 1–13.
- Matheron, G. (1982). Pour une analyse krigéante des données régionalisées. *Centre de Géostatistique, Report N-732, Fontainebleau*.
- Mayewski, P. A., Frezzotti, M., Bertler, N., Ommen, T. V., Hamilton, G., Jacka, T. H., ... Goodwin, I. (2005). The International Trans-Antarctic Scientific Expedition (ITASE): An overview. *Annals of Glaciology*, *41*, 180–185.
- Medley, B., Joughin, I., Smith, B. E., Das, S. B., Steig, E. J., Conway, H., ... Leuschen, C. (2014, July). Constraining the recent mass balance of Pine Island and Thwaites glaciers, West Antarctica, with airborne observations of snow accumulation. *The Cryosphere*, *8*(4), 1375–1392. Retrieved 2019-05-25, from <https://www.the-cryosphere.net/8/1375/2014/> doi: <https://doi.org/10.5194/tc-8-1375-2014>
- Meyer, M. C. (2008). Inference using shape-restricted regression splines. *The Annals of Applied Statistics*, *2*(3), 1013–1033.
- Molteni, F., Buizza, R., Palmer, T. N., & Petroliagis, T. (1996). The ECMWF ensemble prediction system: Methodology and validation. *Quarterly Journal of the Royal Meteorological Society*, *122*(529), 73–119.
- Neal, R. (1998). Regression and classification using Gaussian process priors. *Bayesian Statistics*, *6*, 475.
- Ortiz-Bobea, A., & Tack, J. (2018). Is another genetic revolution needed to offset climate change impacts for us maize yields? *Environmental Research Letters*, *13*(12), 124009.
- Paciorek, C. J. (2010). The importance of scale for spatial-confounding bias and precision of spatial regression estimators. *Statistical Science*, *25*(1), 107.
- Pawson, S., Labitzke, K., & Leder, S. (1998). Stepwise changes in stratospheric temperature. *Geophysical research letters*, *25*(12), 2157–2160.

- Ramsay, J. O. (1988). Monotone regression splines in action. *Statistical Science*, 3(4), 425–441.
- Salamatin, A. N., Lipenkov, V. Y., Barnola, J. M., Hori, A., Duval, P., & Hondoh, T. (2009). Snow/ice densification in polar ice sheets. *Low Temperature Science*, 68(Supplement), 195–222.
- Schofield, M. R., Barker, R. J., Gelman, A., Cook, E. R., & Briffa, K. R. (2016, January). A Model-Based Approach to Climate Reconstruction Using Tree-Ring Data. *Journal of the American Statistical Association*, 111(513), 93–106. Retrieved 2020-09-02, from <https://doi.org/10.1080/01621459.2015.1110524> (Publisher: Taylor & Francis _eprint: <https://doi.org/10.1080/01621459.2015.1110524>) doi: 10.1080/01621459.2015.1110524
- Seidel, D. J., & Lanzante, J. R. (2004). An assessment of three alternatives to linear trends for characterizing global atmospheric temperature changes. *Journal of Geophysical Research: Atmospheres*, 109(D14).
- Shepherd, A., Gilbert, L., Muir, A. S., Konrad, H., McMillan, M., Slater, T., ... Engdahl, M. E. (2019). Trends in Antarctic Ice Sheet Elevation and Mass. *Geophysical Research Letters*, 46(14), 8174–8183. Retrieved 2020-09-17, from <https://agupubs.onlinelibrary.wiley.com/doi/abs/10.1029/2019GL082182> (_eprint: <https://agupubs.onlinelibrary.wiley.com/doi/pdf/10.1029/2019GL082182>) doi: 10.1029/2019GL082182
- Smith, B., Fricker, H. A., Gardner, A. S., Medley, B., Nilsson, J., Paolo, F. S., ... Zwally, H. J. (2020, June). Pervasive ice sheet mass loss reflects competing ocean and atmosphere processes. *Science*, 368(6496), 1239–1242. Retrieved 2020-09-17, from <https://science.sciencemag.org/content/368/6496/1239> (Publisher: American Association for the Advancement of Science Section: Report) doi: 10.1126/science.aaz5845
- Spiegelhalter, D. J., Best, N. G., Carlin, B. P., & Van Der Linde, A. (2002). Bayesian measures of model complexity and fit. *Journal of the Royal Statistical Society: Series B (Statistical Methodology)*, 64(4), 583–639.
- Tanner, M. A. (1996). *Tools for statistical inference* (3rd ed.). Springer-Verlag New York.

- Tebaldi, C., & Lobell, D. (2008). Towards probabilistic projections of climate change impacts on global crop yields. *Geophysical Research Letters*, *35*(8).
- Tebaldi, C., & Sansó, B. (2009). Joint projections of temperature and precipitation change from multiple climate models: a hierarchical bayesian approach. *Journal of the Royal Statistical Society: Series A (Statistics in Society)*, *172*(1), 83–106.
- Teh, Y. W., Seeger, M., & Jordan, M. I. (2005). Semiparametric latent factor models. *AISTATS 2005*, 333.
- Tomé, A., & Miranda, P. (2004). Piecewise linear fitting and trend changing points of climate parameters. *Geophysical Research Letters*, *31*(2).
- Vehtari, A., Gelman, A., & Gabry, J. (2017). Practical Bayesian model evaluation using leave-one-out cross-validation and WAIC. *Statistics and computing*, *27*(5), 1413–1432.
- Verjans, V., Leeson, A. A., Nemeth, C., Stevens, C. M., Kuipers Munneke, P., Noël, B., & van Wessem, J. M. (2020). Bayesian calibration of firn densification models. *The Cryosphere Discussions*, 1–23.
- Wang, C., Wang, S., Fu, B., Li, Z., Wu, X., & Tang, Q. (2017, January). Precipitation gradient determines the tradeoff between soil moisture and soil organic carbon, total nitrogen, and species richness in the Loess Plateau, China. *Science of The Total Environment*, *575*, 1538–1545. Retrieved 2020-09-02, from <http://www.sciencedirect.com/science/article/pii/S0048969716322136> doi: 10.1016/j.scitotenv.2016.10.047
- Watanabe, S. (2010). Asymptotic equivalence of Bayes cross validation and widely applicable information criterion in singular learning theory. *Journal of Machine Learning Research*, *11*(Dec), 3571–3594.
- Wessem, J. M. v., Berg, W. J. v. d., Noël, B. P. Y., Meijgaard, E. v., Amory, C., Birnbaum, G., ... Broeke, M. R. v. d. (2018, April). Modelling the climate and surface mass balance of polar ice sheets using RACMO2 – Part 2: Antarctica (1979–2016). *The Cryosphere*, *12*(4), 1479–1498. Retrieved 2020-06-05, from <https://www.the-cryosphere.net/12/1479/2018/> (Publisher: Copernicus GmbH) doi: <https://doi.org/10.5194/tc-12-1479-2018>

White, P. A., Keeler, D. G., & Rupper, S. (2020). Hierarchical integrated spatial process modeling of monotone west antarctic snow density curves. *arXiv preprint arXiv:2001.05520*.

White, P. A., Reese, C. S., Christensen, W. F., & Rupper, S. (2019). A model for Antarctic surface mass balance and ice core site selection. *Environmetrics*, 30(8), e2579.

Zhang, H. (2004). Inconsistent estimation and asymptotically equal interpolations in model-based geostatistics. *Journal of the American Statistical Association*, 99(465), 250–261.

A Model Comparison

Because the density measurements are bounded below, we consider truncated Normal and truncated Student’s t error distributions for these data. To account for expedition differences, as well as the length of the core used to obtain each density measurement, we consider hierarchical and weighted models for the scale of the error distribution. Our model comparison question here is which components of this model are beneficial. For this comparison, we find that the truncated Student’s t distribution with weighted, hierarchical scale parameters has the lowest WAIC (See Table 2).

We consider eight possible cross-covariance specifications for the 12 spatially-varying parameters used to model these data that can be written in the form (see [Álvarez & Lawrence, 2011](#); [Banerjee et al., 2014](#), for review):

$$\Sigma = (\mathbf{\Lambda} \otimes \mathbf{I}) \text{BlockDiag}(\mathbf{R}_1, \dots, \mathbf{R}_r) (\mathbf{\Lambda}^T \otimes \mathbf{I}). \quad (12)$$

In this model, $\mathbf{\Lambda}$ controls between-parameter dependence and is $12 \times r$, where $r \leq 12$. To govern spatial dependence, we use correlation matrices $\mathbf{R}_1, \dots, \mathbf{R}_{12}$, where the i th row and j th column of the k th correlation matrix is $(\mathbf{R}_k)_{i,j} = \exp(-\phi_k d(\mathbf{s}_{ij}, \mathbf{s}_l))$. Here, we use $d(\mathbf{s}_{ij}, \mathbf{s}_l)$ as the great-circle distance; however, other distance metrics may be just as effective in this application (e.g., the chordal distance). We consider the following possibilities:

Independent: If (a) $\mathbf{\Lambda}$ is 12×12 identity matrix, then we assume no between-parameter dependence and $\Sigma = \text{BlockDiag}(\mathbf{R}_1, \dots, \mathbf{R}_{12})$.

Separable: If we let $r = 12$ and $\mathbf{R} = \mathbf{R}_1 = \mathbf{R}_2 = \dots = \mathbf{R}_{12}$, then we get a separable model $\Sigma = (\mathbf{\Lambda}\mathbf{\Lambda}^T) \otimes \mathbf{R}$. This model is often called the intrinsic model of coregionalization (see [Matheron, 1982](#)). In this model, we assume that the spatial patterns for all parameters is similar and can be represented using a single correlation function .

Latent Factor/Coregionalization: If $r < 12$, then we get latent factor model and we cannot simplify (12). For a nice discussion of these models, see [Teh et al. \(2005\)](#). This model assumes that the we can describe the 12-dimensional spatial process using a lower-rank space. If we let $r = 12$ and let $\mathbf{\Lambda}$ be lower-triangular, then we get the linear model of coregionalization and we cannot simplify (12) (see [Grzebyk & Wackernagel, 1994](#), for early reference). In this model, we do not assume any rank-reduction.

Richer cross-covariance functions (see, e.g., [Gneiting et al., 2010](#); [Genton & Kleiber, 2015](#)) or non-stationary cross-covariance functions (see, e.g., [Kleiber & Nychka, 2012](#)) are often beneficial. However, with $n_s = 56$ sites, we have limited ability to estimate complicated spatial models and find that more complicated spatial models perform worse for this data. Moreover, many models have limited parameter identifiability; therefore, we argue that these cross-covariance functions offer sufficient flexibility.

Because the spatially-varying HL model (6) is piecewise linear, we explore various specification of the smoothed HL model (7) to see whether they improve upon (6). Specifically, we use a cubic polynomial, quadratic splines (with one, two, or three knots), and cubic splines (with one, two, or three knots). The results of the model comparison are given in [Table 4](#). We use the cubic spline with two knots because it has the lowest WAIC; however, all spline models with two or more knots are comparable in terms of WAIC.

B Extended Posterior Analysis

In [Figure 9](#), we plot the mean empirical between-parameter correlation taken from the 56 sites. We examine the correlation on the transformed parameter scale to decrease the effects of large values. There are many strong correlations. We note only a few. The intercept and critical densities are all positively correlated. Interestingly, the log-transformed pre-exponentiation factors for the first and fourth stages have a strong negative correlation with the critical densities.

We give violin plots for site-specific posterior distribution in Figures 10, 11, and 12. From these plots, we see three clear and unsurprising patterns: (1) Arrhenius parameters that govern densities at shallower depths have lower posterior variance compared to parameters for deeper densification stages. (2) Cores with more observations have better resolved posterior distributions. (3) Cores distant from other cores have higher variance.

In Figure 13, we plot the interquartile range of each spatially-varying parameter over the convex hull of our dataset. We use the interquartile range because untransformed parameters have extreme values. In general, uncertainty is highest near the boundaries of our interpolation region and far from drilled cores.

Estimate Description	Function of Parameters	Previous Estimate Posterior Quantile	Mean	Median	Std. dev.	5%	95%
Surface Density	$\frac{\rho_L \exp(\gamma_\alpha)}{1 + \exp(\gamma_\alpha)}$	—	0.365	0.364	0.046	0.291	0.442
1st-stage A	$\exp(\gamma_{A_1})$	0.577	10.810	10.650	1.892	7.978	14.150
1st-stage E	$\exp(\gamma_{E_1})$	0.756	9.46e3	9.38e3	1.07e3	7.78e3	1.13e4
2nd-stage A	$\exp(\gamma_{A_2})$	0.511	578.700	572.800	80.540	457.900	719.700
2nd-stage E	$\exp(\gamma_{E_2})$	0.505	2.14e4	2.14e4	1.47e3	1.91e4	2.39e4
1st Critical Density	$f_1(\rho_1)$	0.835	0.524	0.522	0.026	0.484	0.571
2nd Critical Density	$f_2(\rho_2)$	0.267	0.739	0.741	0.014	0.714	0.760
3rd Critical Density	$f_3(\rho_3)$	0.071	0.846	0.847	0.010	0.828	0.860

Table 1: Posterior summaries of untransformed hierarchical parameters.

Truncated Distribution	Weighting	Hierarchical	WAIC	Relative WAIC	WAIC SE
Normal	Yes	Yes	-73234.89	3410.35	338.17
Student's- t	No	No	-73740.73	2904.52	272.37
Student's- t	Yes	No	-75297.33	1347.91	275.06
Student's- t	No	Yes	-75775.72	869.53	272.71
Student's-t	Yes	Yes	-75791.80	853.44	272.33

Table 2: WAIC for models differing in their error distribution.

Cross-Covariance Function	WAIC	Relative WAIC	WAIC SE
Separable GP	-75791.80	853.44	272.33
Independent GP	-75766.30	878.94	272.82
2 Latent Factors	-74572.49	2072.76	267.38
4 Latent Factors	-75654.19	991.06	268.43
6 Latent Factors	-75600.94	1044.31	270.75
8 Latent Factors	-75606.62	1038.62	270.62
10 Latent Factors	-75776.52	868.72	271.53
Coregionalization (12 Latent Factors)	-75690.65	954.59	270.70

Table 3: WAIC for models differing by the cross-covariance of the transformed parameters.

Model for $\mathbf{h}_\theta^+(s_{ij}, x)$	Number of Knots	WAIC	Relative WAIC	WAIC SE
None	—	-75791.80	853.44	272.33
Cubic Polynomial	—	-75822.69	822.56	272.95
Quadratic Spline	1	-76383.12	262.13	278.51
Quadratic Spline	2	-76645.25	0.00	278.69
Quadratic Spline	3	-76601.84	43.41	279.04
Cubic Spline	1	-76541.38	103.87	278.77
Cubic Spline	2	-76625.65	19.60	280.73
Cubic Spline	3	-76617.85	27.40	280.09

Table 4: WAIC for models differing by the smooth nonlinear adjustment to the piecewise linear model.

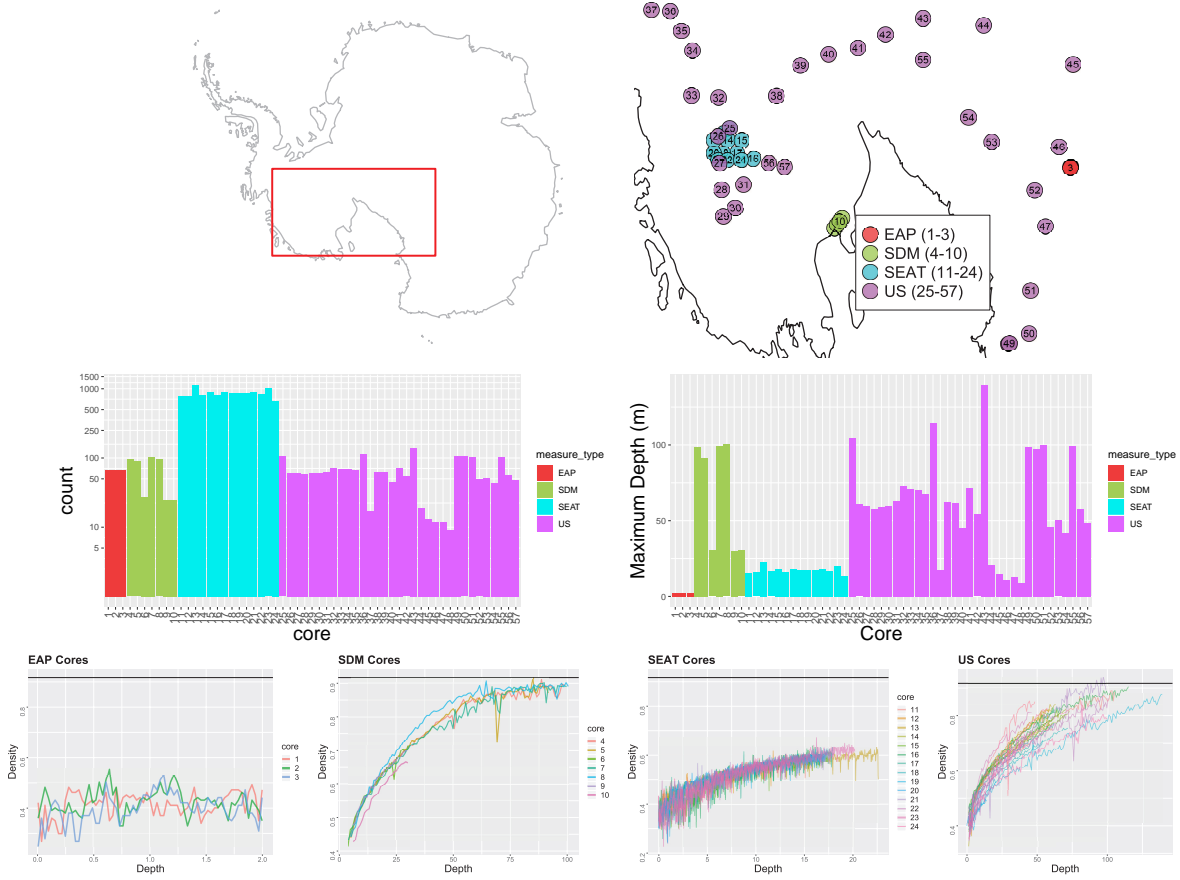


Figure 1: (Top-Left) Region of Antarctica where snow/ice cores are located. (Top-Right) Location of core sites with colors indicating measurement type. (Middle-Left) The number of density measurements at each core, and (Middle-Right) Maximum depth in m obtained by each core. (Bottom) Density measurements over depth by core, grouped by expedition. Note that the depth scales of these measurement types differ greatly. The horizontal line indicates the density of solid ice.

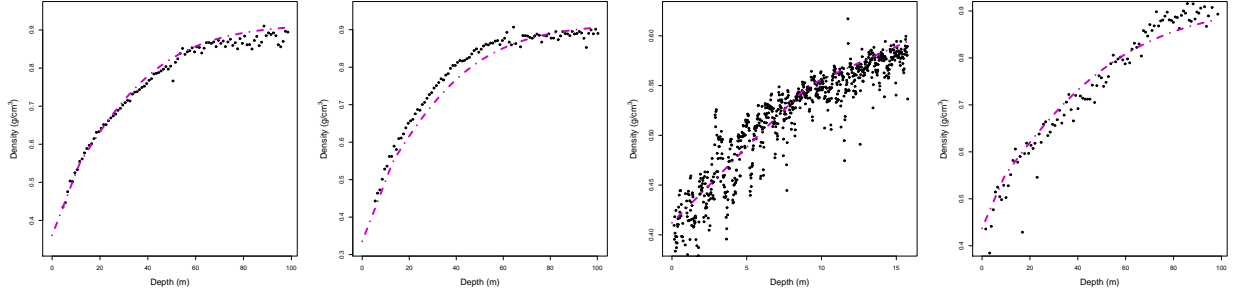


Figure 2: HL model fit to core (Left) 4, (Middle Left) 8, (Middle Right) 12, (Right) 49.

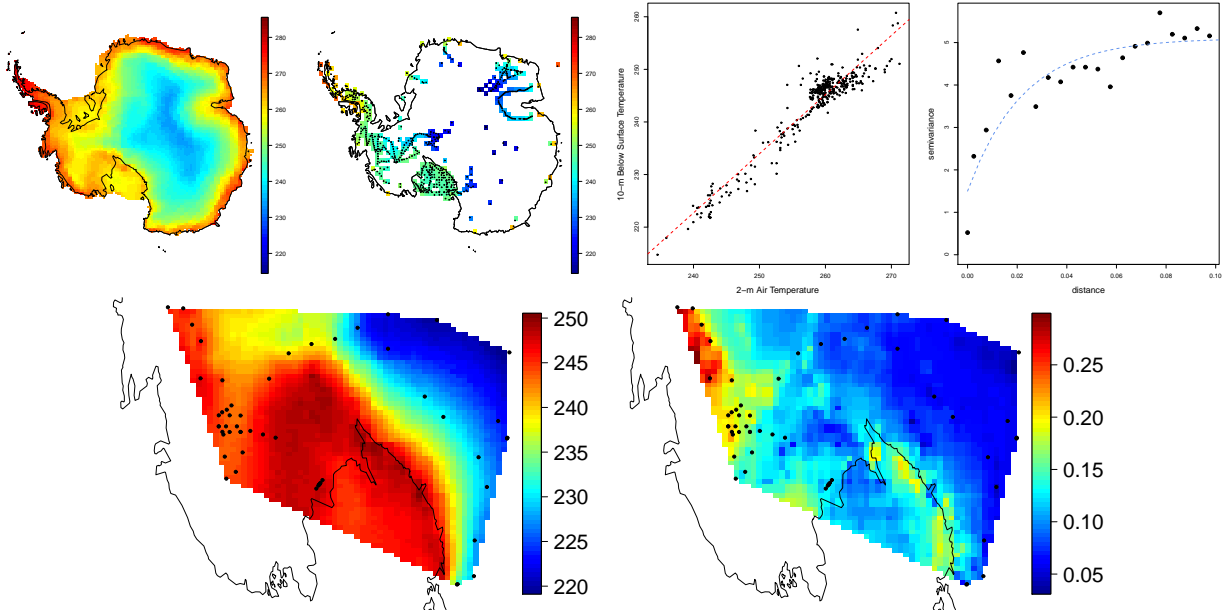


Figure 3: (Top-Left) Smoothed ERA-Interim 2-m air temperature averaged from 1979-2014. (Top-Center-Left) Temperature data 10-m below the surface. (Top-Center-Right) Relationship between nearest 2-m air temperature to observed temperature data 10-m below the surface. (Top-Right) Semivariogram for the residuals for temperature 10-m below the surface with a fit to an exponential semivariogram. (Bottom-Left) Temp-10 below (Bottom-Right) SMB

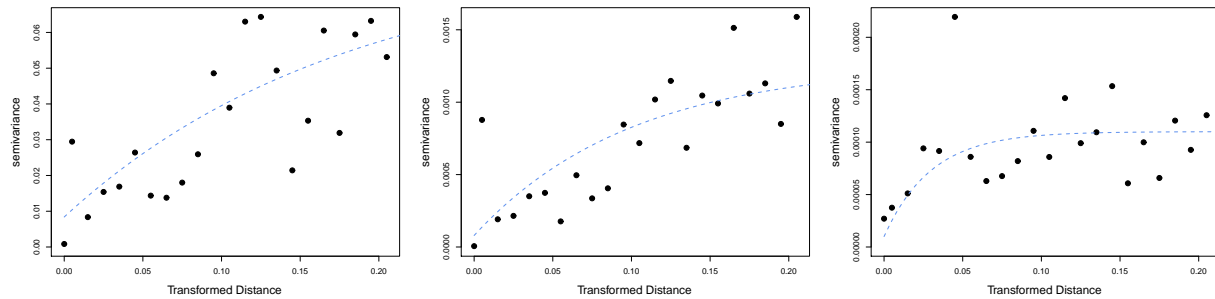


Figure 4: Empirical binned semivariogram for site-specific (Left) intercepts, (Center) First-stage Arrhenius constant, and (Right) Second-stage Arrhenius constants of the HL model. All binned semivariograms are plotted with a fit to an exponential semivariogram.

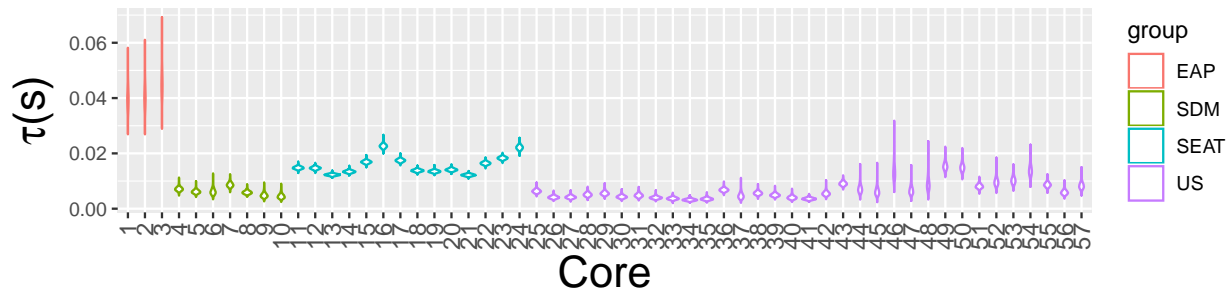


Figure 5: Posterior distributions for core-specific scale parameters.

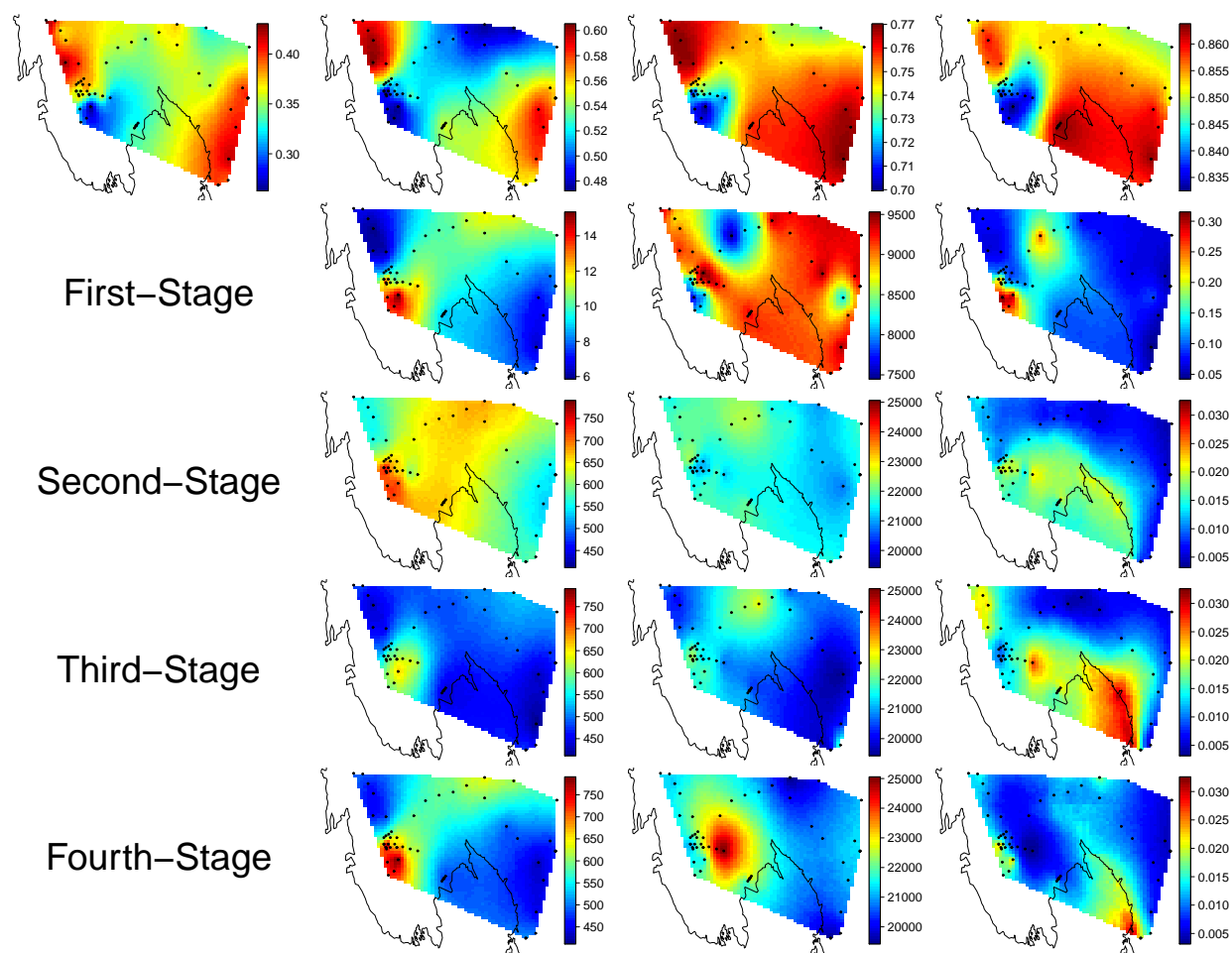


Figure 6: (Row 1) Posterior median for surface density and the three critical densities, all in g/cm^3 , from left to right. (Rows 2-5) Posterior medians for $A_l(\mathbf{s})$, $E_l(\mathbf{s})$, and $k_l(\mathbf{s}) = A_l(\mathbf{s}) \exp\left(-\frac{E_l(\mathbf{s})}{RT(\mathbf{s})}\right)$, for stages $l = 1, 2, 3, 4$. Second, third, and fourth stages share the same scale to allow visual comparison.

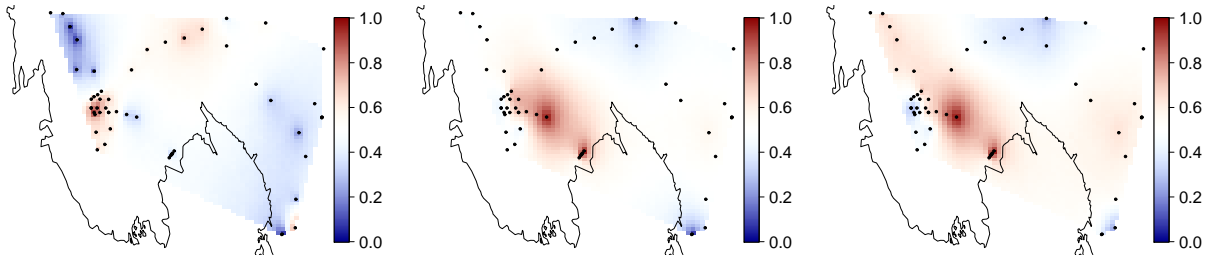


Figure 7: Posterior probability of (Left) $k_2(\mathbf{s}) > k_3(\mathbf{s})$, (Center) $k_2(\mathbf{s}) > k_4(\mathbf{s})$, and (Right) $k_3(\mathbf{s}) > k_4(\mathbf{s})$. Both small and large probabilities indicate differences between adjacent stages. The dotted line is the convex hull of our data.

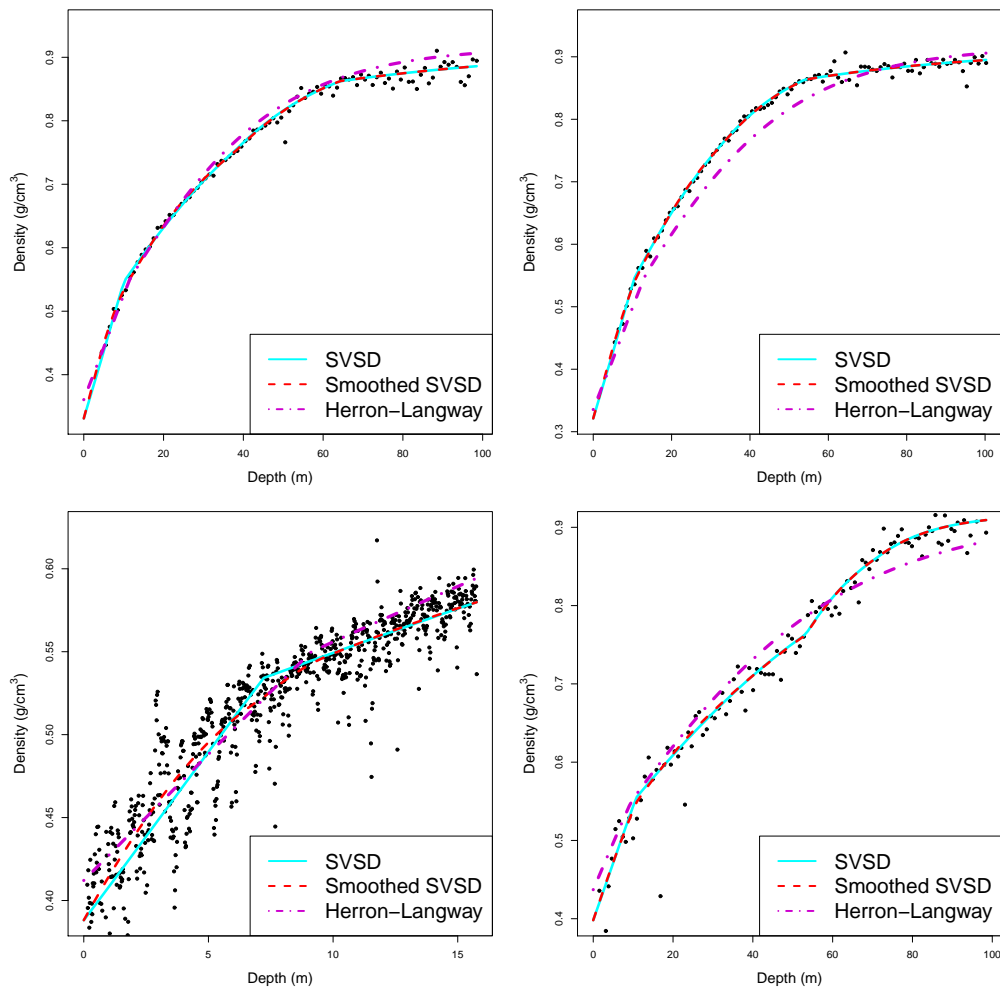


Figure 8: A comparison of the HL, SVSD, and the smoothed SVSD models for cores 4, 8, 12, and 49, from top-left to bottom-right. For the SVSD and the smoothed SVSD models, we illustrate the model fit using the posterior mean.

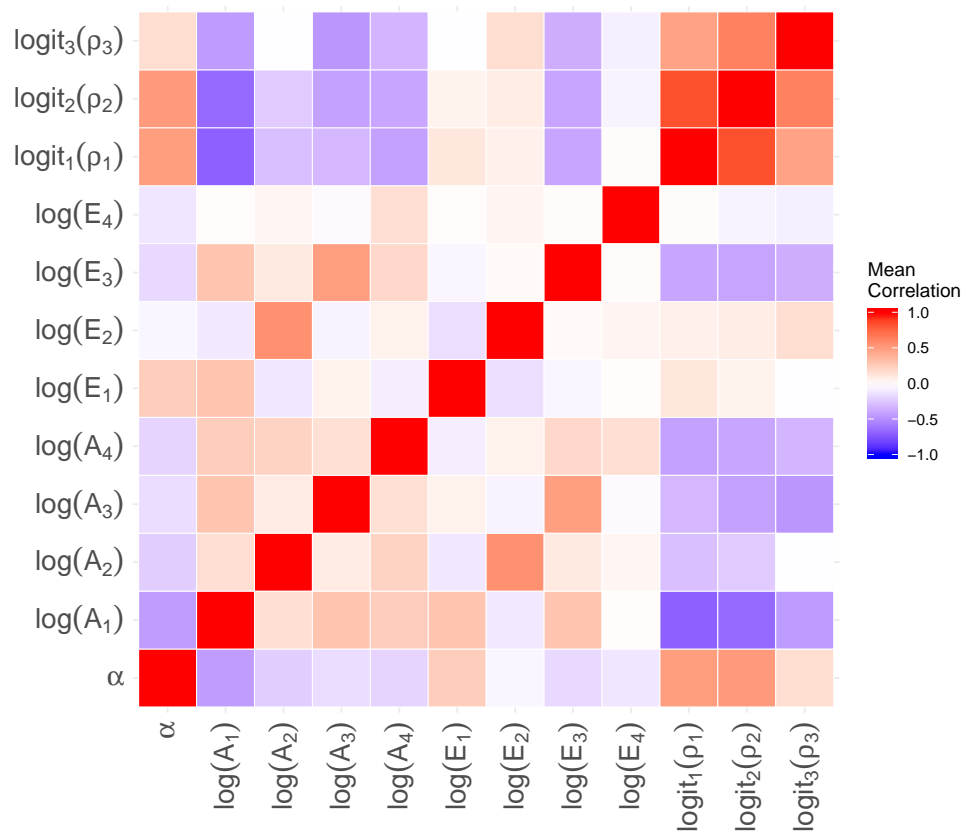


Figure 9: Empirical average between-parameter correlation estimated from 56 site-specific parameters.

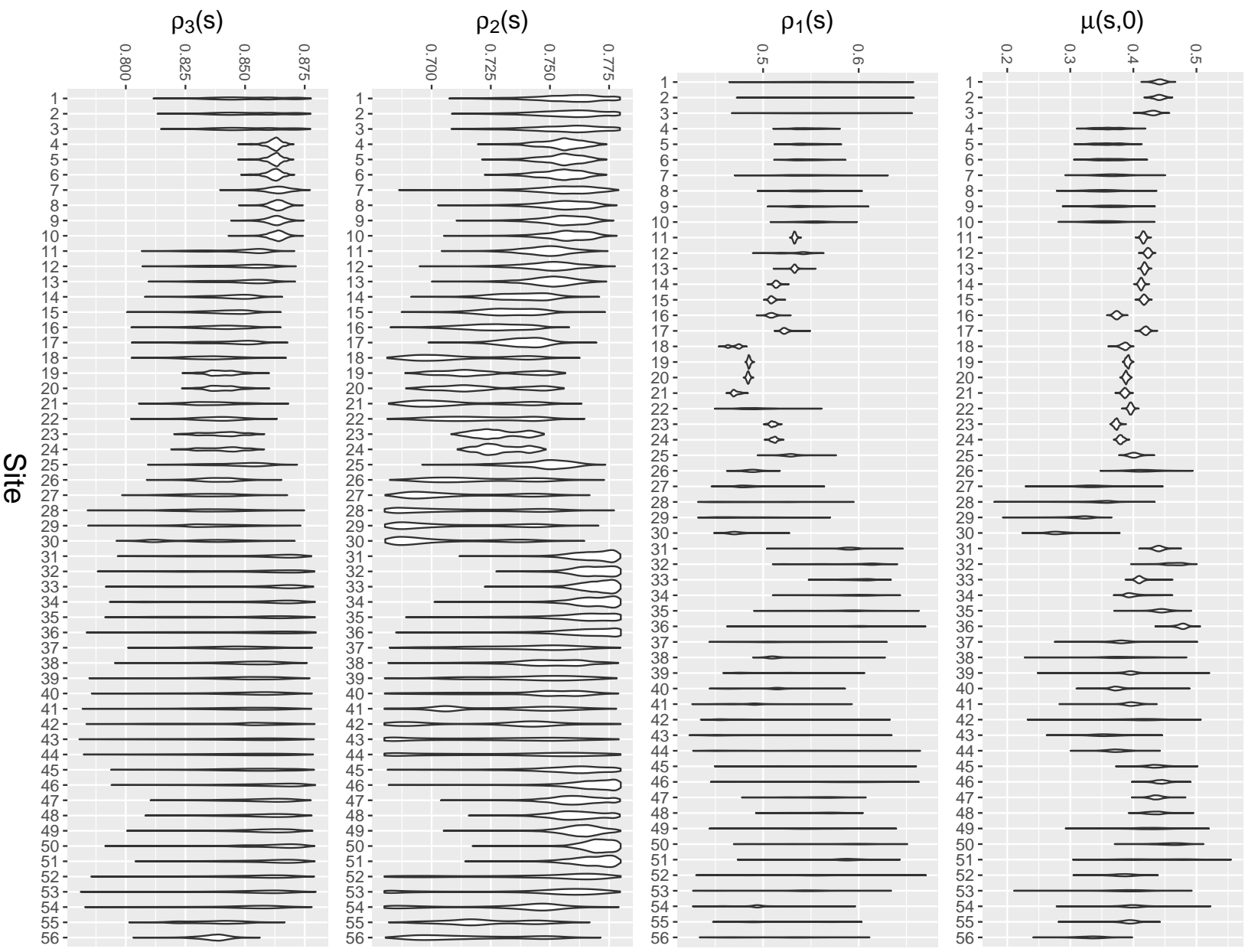


Figure 10: Posterior distributions for site-specific intercepts and critical densities.

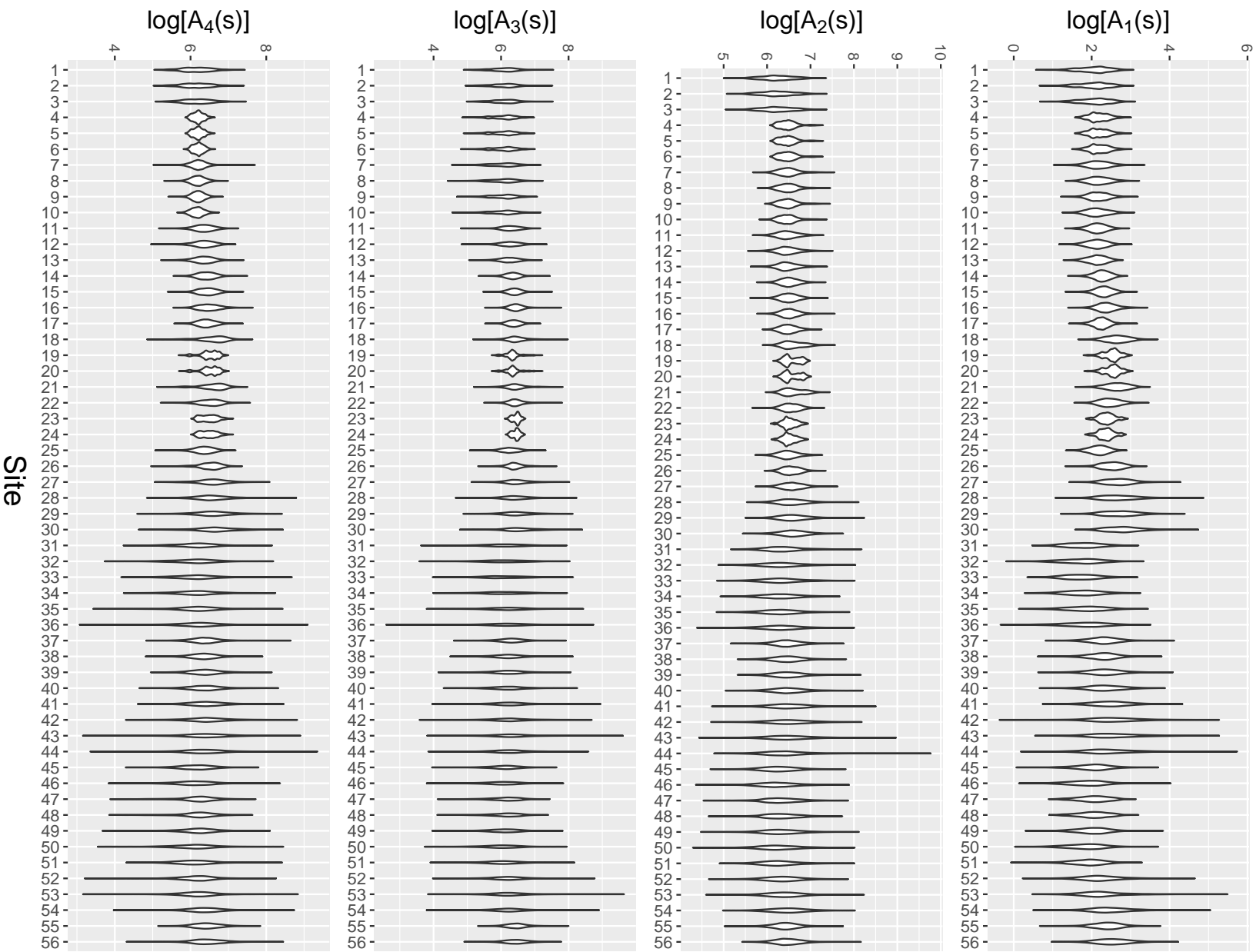


Figure 11: Posterior distributions for site-specific log-transformed pre-exponentiation factors.

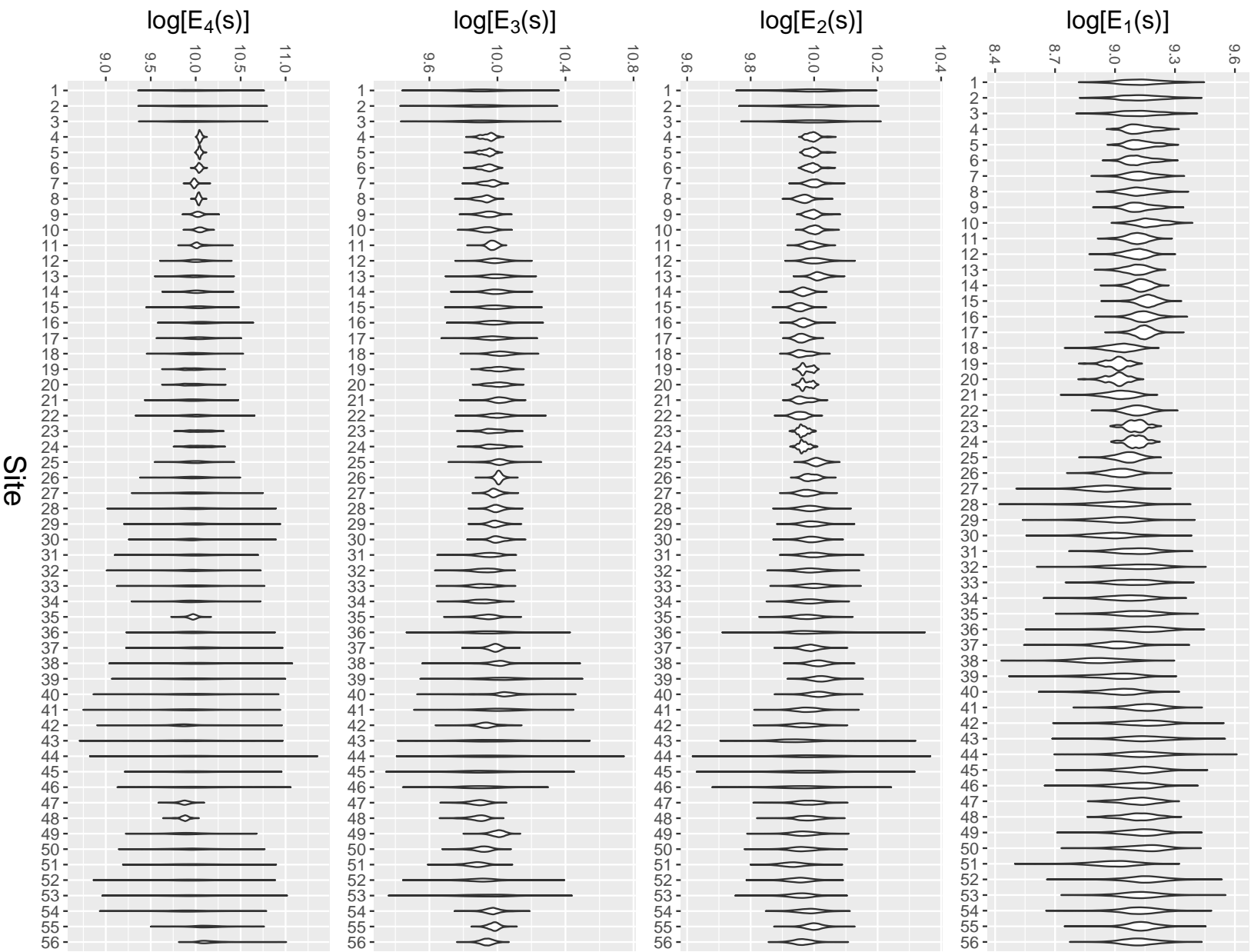


Figure 12: Posterior distributions for site-specific log-transformed energies of activation.

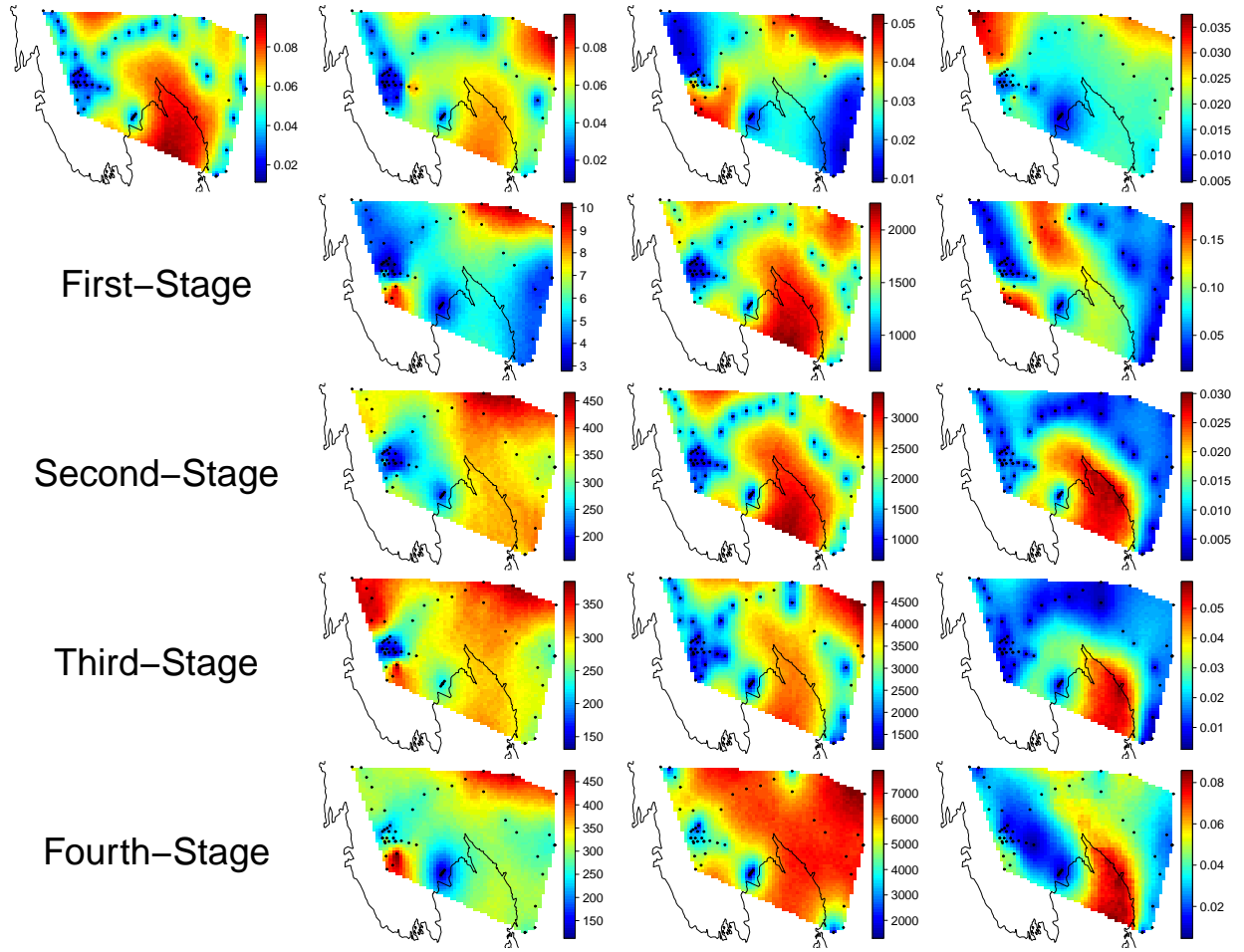


Figure 13: Interquartile range for (Row 1) surface density and the three critical densities, all in g/cm^3 , from left to rightmm. Interquartile range for (Rows 2-5) $A_l(\mathbf{s})$, $E_l(\mathbf{s})$, and $k_l(\mathbf{s}) = A_l(\mathbf{s}) \exp\left(-\frac{E_l(\mathbf{s})}{RT(\mathbf{s})}\right)$, for stages $l = 1, 2, 3, 4$.